iScience

CellPress

Article

Alternating-Magnetic-Field-Mediated Wireless Manipulations of a Liquid Metal for Therapeutic Bioengineering

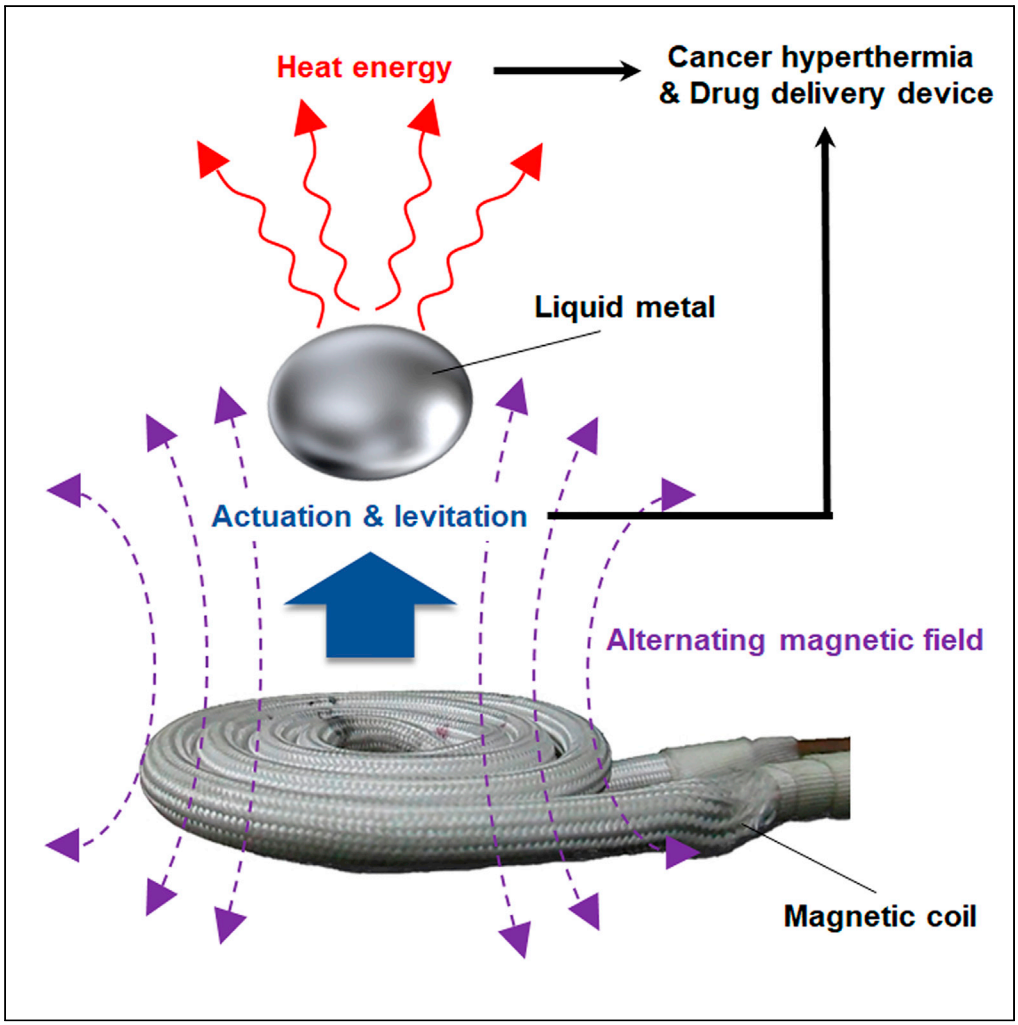

Yue Yu, Eijiro Miyako

e-miyako@aist.go.jp

HIGHLIGHTS

LM is actuated and levitated via AMF

LM heats up with application of low-frequency AMFs

AMF-driven LM exothermicity shows *in vitro* and *in vivo* cancer hyperthermia

Pill-shaped LM microdevice displays controllable drug delivery systems

Yu & Miyako, iScience *3*, 134–148
May 25, 2018
https://doi.org/10.1016/j.isci.2018.04.012

iScience

CellPress

Article

Alternating-Magnetic-Field-Mediated Wireless Manipulations of a Liquid Metal for Therapeutic Bioengineering

Yue Yu[1] and Eijiro Miyako[1,2,*]

SUMMARY

As emergent multifunctional materials, room temperature liquid metals (LMs) display many unique properties. Here we show that applying an external alternating magnetic field (AMF) to an LM induces various physical phenomena, such as exothermic behavior, controlled locomotion, electromagnetic levitation, and transformations of the LMs between different morphologies and configurations, in a non-contact manner. Additional interesting therapeutic bioengineering applications of LMs demonstrated herein include *in vitro* and *in vivo* effective cancer magnetic hyperthermia via wireless AMF, remote manipulation of a pill-shaped microdevice based on an LM/hydrogel composite, and spatiotemporal controlled release of drug molecules from the microdevice. Overall, as an innovative therapeutic bioengineering technology, this platform and the described performance traits of LMs enable the development of biocompatible smart devices with a wide range of dynamic components that can be wirelessly controlled in a manner that solves issues related to the powering of devices and biocompatibility.

INTRODUCTION

Room temperature liquid metals (LMs), which particularly comprise gallium, gallium-indium eutectic alloys (EGaIn: 75% Ga, 25% In [wt wt^{-1}]), and gallium-indium-tin alloys (Galinstan: 68.5% Ga, 21.5% In, and 10% Sn [wt wt^{-1}]), have received increasing attention as building blocks for the design of functional composite materials because of their remarkable properties, which include superior conductivity, favorable flexibility, and high biocompatibility compared with mercury (Dickey, 2014; Chen et al., 2017, 2018). Remote manipulations of LM morphologies (Tsai et al., 2009; Sheng et al., 2014; Eaker and Dickey, 2016; Gough et al., 2016) are essential techniques for these innovative material applications. However, literature studies describing LM manipulation strategies and their effect on the dynamics of these materials are scarce. Kalantarzadeh et al. reported a pH-imbalance-induced LM pump as a lab-on-a-chip mixer (Zavabeti et al., 2016). Tang et al. investigated the effect of voltage on LM dynamic manipulation (Tang et al., 2014). Basically, the conventional manipulation methods of LM morphologies require contact methods such as the immersion of LMs into harsh acidic or alkaline pH solution and the attachment of an electrode onto the LM surface. The wireless and noninvasive manipulation of functional LMs operating in physiological environments has attracted considerable research interest (Chechetka et al., 2017; Yu and Miyako, 2017). For instance, Tang et al. and Zhang et al. studied wireless controlled manipulations of LM marbles by electrochemical applications (Tang et al., 2013a, 2013b; Zhang et al., 2015). Meanwhile, Tan et al. also reported photochemically induced non-contact motion of LM blobs (Tang et al., 2013a, 2013b). Kim et al. investigated magnetic-field-induced LM droplet on-demand manipulation (Kim and Lee, 2015). However, these manipulation methods are essential for physical coating of functional nanoparticles on the surface of LMs for providing driving forces for their movements. In other words, these manipulation behaviors are basically powered by performances of nanoparticles rather than by the original LM properties.

Therapeutic bioengineering is the application of engineering principles and design concepts to medicine and biology for health care purposes. The emerging field of therapeutic bioengineering has the objective of associating different classes of materials to impart functionalities toward the development of advanced devices and enhanced multifunctional modalities in different application fields, including biomedicine and theranostics (Yoo et al., 2011; Avery et al., 2016; Guan et al., 2017). Over the past several decades, the continuous growth of therapeutic bioengineering has brought innovations in the biomedical domain, thus resulting in advancements in the therapeutic, imaging, and diagnostic fields. In particular, the controlled delivery of bioactive agents and the local treatments of diseases are perspectives in the

[1]Department of Materials and Chemistry, Nanomaterials Research Institute (NMRI), National Institute of Advanced Industrial Science and Technology (AIST), Central 5, 1-1-1 Higashi, Tsukuba, Ibaraki 305-8565, Japan

[2]Lead Contact

*Correspondence: e-miyako@aist.go.jp

https://doi.org/10.1016/j.isci.2018.04.012

development of efficient multifunctional therapeutics (Timko et al., 2014; Chin et al., 2017). Recent advances in therapeutic bioengineering have enabled systems and devices that respond to external stimuli such as acoustic, electromagnetic induction, or optical signals (Tufail et al., 2010; Wykes et al., 2012; Chin et al., 2017). However, these physical fields are largely absorbed and scattered by tissue and similarly require a conduit for their medical treatments. By contrast, low-frequency alternating magnetic fields (AMFs) (100 kHz–1 MHz) can deeply penetrate into the body without substantial attenuation (Young et al., 1980; Chen et al., 2015). LMs can be integrated all-in-one and provide an innovative tool for the bioengineering of therapeutic properties under physical control (Tsai et al., 2009; Sheng et al., 2014; Lu et al., 2015; Eaker and Dickey, 2016; Gough et al., 2016). Although electrical and oxidation-reduction controls of LMs have been extensively investigated, magnetic manipulations of promising LMs have not been sufficiently explored. Given these aims, the next logical step is to test these dynamic controls of LMs under AMFs suitable for various therapeutic bioengineering applications.

In this work, we examine the AMF-driven LM physiochemical properties to show that an EGaIn LM without any coating of nanoparticles exhibits unique properties under wireless AMF induction, enabling, for example, controlled directional locomotion or electromagnetic levitation. In addition, AMFs can be used to effectively eliminate tumors *in vitro* and *in vivo* via EGaIn, which dissipates heat via eddy currents. Finally, we demonstrate AMF control of the wireless dynamics of a pill-shaped microdevice composed of an LM and agarose hydrogel and trigger drug release from the device.

RESULTS

AMF-Modulated Three-Dimensional LM Manipulations

Accidently, we discovered the possibility of manipulating the LM using an AMF. A glass vial containing 100 μL of the LM was positioned above the center of a magnetic coil. Under an AMF (250 A m^{-1}, 245 kHz), the LM droplet instantly exhibited a "stand-up" shape with a 9-fold increase in height. Moreover, this deformation behavior was reversible via ON-OFF modulation of the AMF power (Figure 1A). Stepwise motions of an LM blob in the horizontal direction were also achieved on a glass slide by this ON-OFF switching of the AMF induction (Figure 1B and Video S1). Conventional supermagnetostrictive materials (e.g., Galfenol [$Fe_{100-x}Ga_x$] and Terfenol-D [$Tb_{0.3}Dy_{0.7}Fe_{1.92}$]) are known to exhibit axial displacement during magnetostriction (Galfenol, ca. 200–300 ppm [Clark et al., 2000]; Terfenol-D, ca. 1500–2000 ppm [Clark and Belson, 1972]). Visible vertical displacement of a Terfenol-D pillar was not observed after AMF induction because of its slight magnetostriction (Figure 1C).

Because the LM adhered to the vial bottom, wherein its movement was disturbed by its oxide skin, we added 30 μL of water around it to introduce a slip layer between the LM and the bottom surface and then repeated the same experiment (Khan et al., 2014). In this case, by momentary ON-OFF switching of the AMF (250 A m^{-1}, 245 kHz), the water-surrounded LM (40 μL) jumped (Figure 2A) and bounced to the edge of the glass dish (Video S2). The LM surface temperature increased to only 31.9°C from room temperature (Figure S1) during this process, suggesting that most of the energy from the AMF was converted into kinetic energy. When the position of the LM droplets was shifted approximately 1 cm from the coil center, the same power of AMF pulse stimulation (250 A m^{-1}, 245 kHz) drove all the droplets to the edge against the direction of the coil center but without the droplets exhibiting a jumping motion (Figure 2B). The movement distances of an LM could be easily controlled just by adjusting the external AMF power (Figure S2). In general, it is difficult to manipulate solid-state materials in narrow and small spaces because of their inflexible behavior. The rigid nature of solid-state materials might restrict their ability to introduce changes in the applications to respond to the function as a building block for creating a flexible soft material. Thus to examine the potential flexibility of LM blobs in tight space, a narrow glass test tube (ca. 5 mm in diameter) was utilized to investigate the deformability of LM via AMF induction. An LM blob (30 μL, ca. 5 mm in diameter) was filled into a glass test tube with and without water. Movements of LM blobs could be successfully controlled in glass test tubes regardless of the presence or absence of water (Figures S3A and S3B). We also confirmed the flexibility of an AMF-driven LM droplet using a Pasteur pipette with a relatively narrow tip (ca. 2.5 mm in diameter). An LM droplet (30 μL, ca. 5 mm in diameter) was vertically filled into the pipette. Because the diameter of the droplet was larger than that of the pipette tip, it is reasonable to think that the LM got stuck at the outlet of the tip. However, when AMF is induced, the droplet speedily comes out of the tip and eventually drops down (Figure S3C and Video S3). These results indicate that the AMF can induce robust movement of the LM in three-dimensional space and that such motion is related to the direction of the magnetic field relative to the

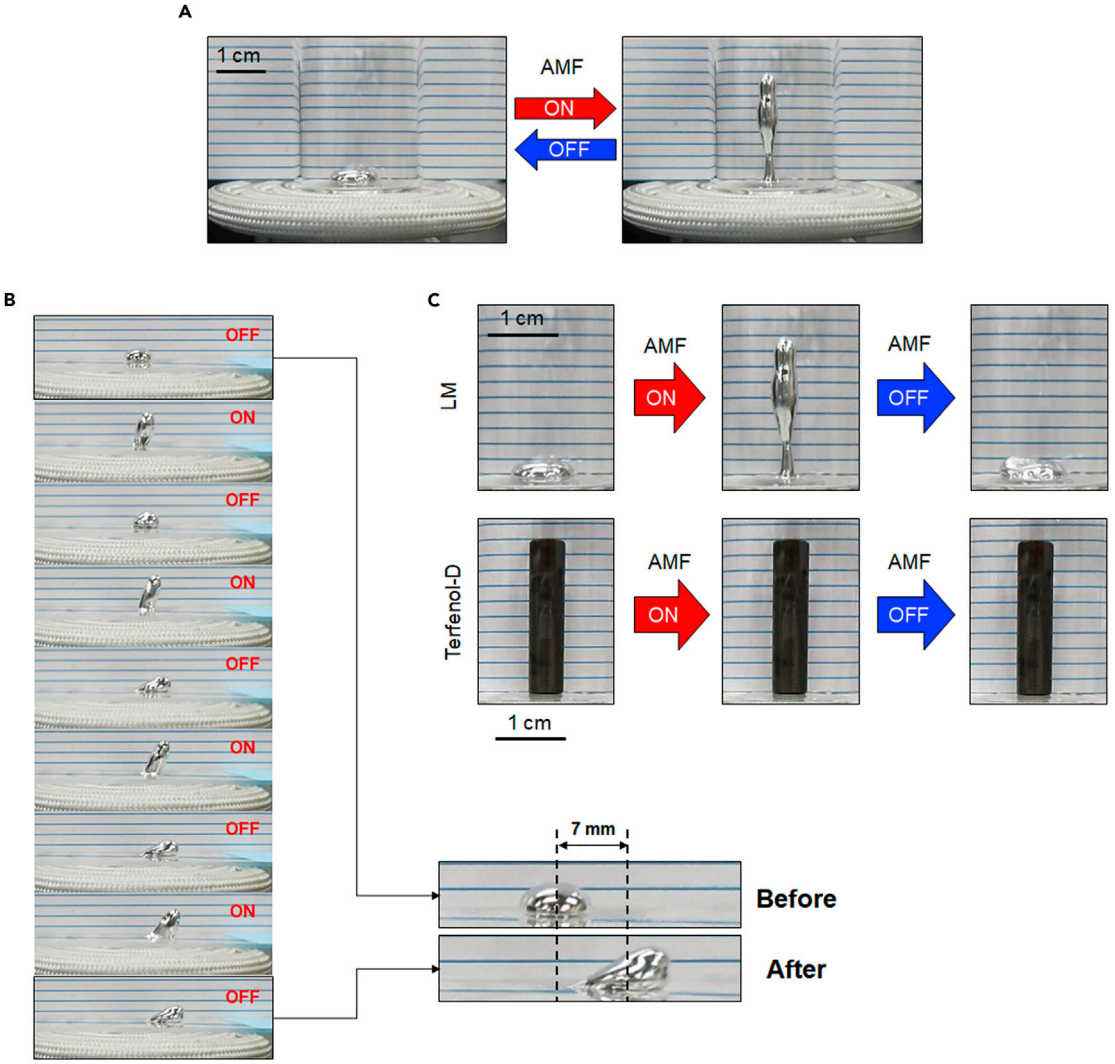

Figure 1. AMF-Induced Manipulation of LM Blobs

(A) AMF-modulated reversible deformation behavior of the LM. LM volume: 100 μL; AMF strength: 250 A m^{-1}, 245 kHz.

(B) Horizontal stepwise motions of an LM blob by ON-OFF switching mode of AMF induction. LM volume: 100 μL; AMF strength: 270 A m^{-1}, 245 kHz.

(C) Morphological changes of LM and Terfenol-D after AMF induction. LM volume: 100 μL; Terfenol-D volume: 707 μL; AMF strength: 250 A m^{-1}, 245 kHz.

position of the LM. We speculate that these dynamic transformations and controllable manipulation behaviors from simple AMF-induced LMs represent an innovation as an alternative to conventional ferrofluids, giant magnetostrictive materials (Clark and Belson, 1972; Clark et al., 2000), and extreme-environment elastic materials (Swallow et al., 2017).

AMFs are well known to induce eddy currents in closed loops within a conductor. Because of Lenz's law, the created currents induce another magnetic field that opposes the external AMF, appearing as a repulsion force (Lorentz force) on the conductor (Thess et al., 2006). The magnitude of the force is proportional to the strength of the magnetic field. Because the magnetic field is most intense at the coil center, eddy currents in the LM render a repulsive force of sufficient magnitude for the LM to overcome gravity (Figure 2C). Consequently, the LM exhibits a "jumping" action under AMF exposure. However, when the LM is outside the coil center, where the AMF direction is inclined and its strength is reduced, the LM cannot be elevated because the vertical component of the repulsive force is counteracted by its gravity. Hence, the LM, affected only by the planar component of the repulsive force, moves sideways.

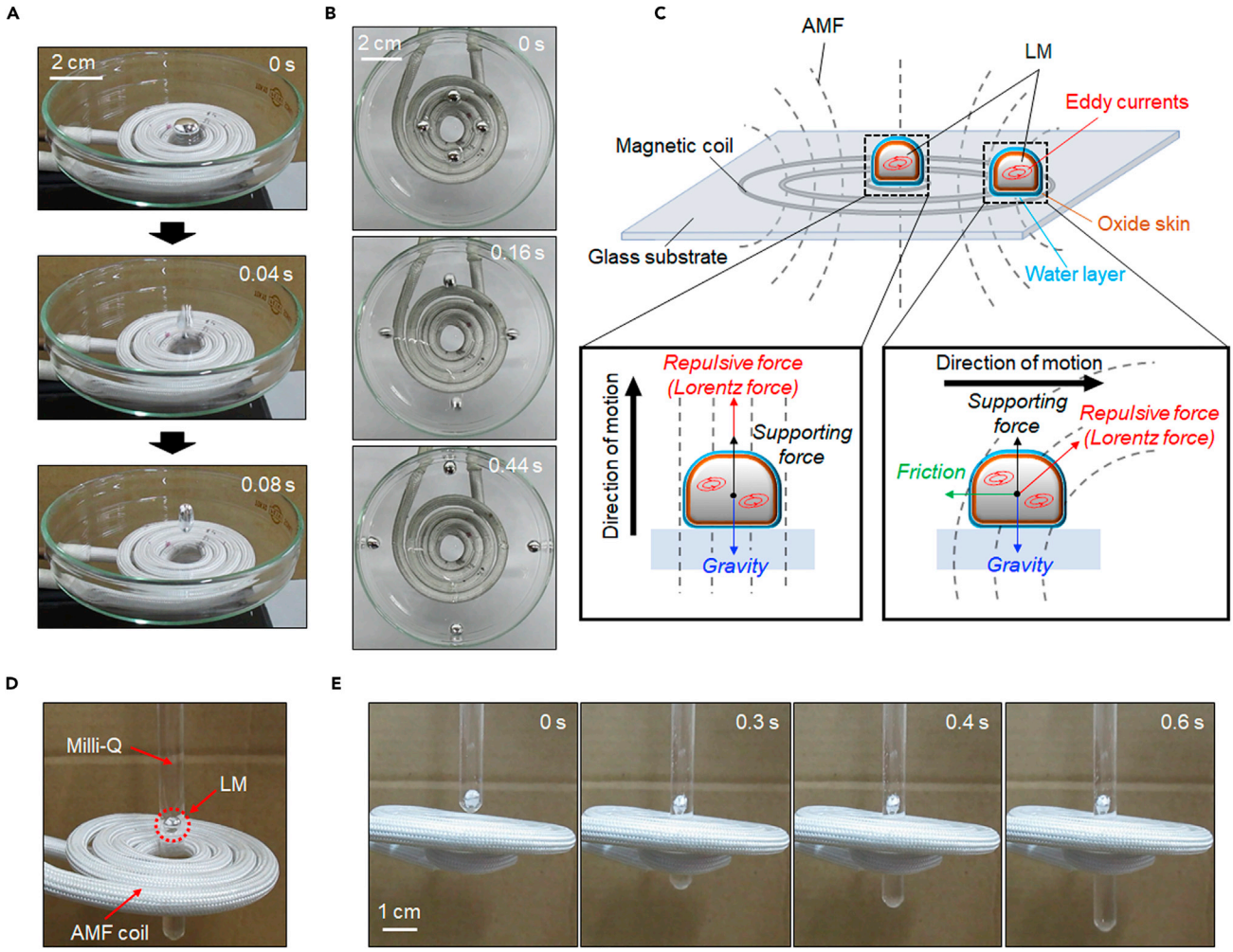

Figure 2. AMF-Modulated Three-Dimensional Locomotion of LM Blobs

(A and B) Sequential snapshots of horizontal (A) and vertical (B) locomotion of the LM (40 μL) manipulated by AMF in air. AMF strength: 250 A m^{-1}, 245 kHz.

(C) Schematic showing the forces affecting the motion of LMs placed in different positions under the AMF.

(D) Quarter-view depiction of the LM levitating over the center of the AMF coil in water.

(E) Time-lapsed electromagnetic levitation images of an LM droplet (40 μL) in water. AMF strength: 250 A m^{-1}, 245 kHz.

Inspired by the aforementioned surprising behaviors, we sought to manipulate the LM locomotion in a steady and consistent manner. We loaded a droplet of LM (40 μL, ca. 0.4 cm in diameter) into a spindly glass test tube (ca. 0.6 cm in diameter and prefilled with deionized water) such that the tube could freely pass through the coil center, as shown in Figure 2D. Upon continuous exposure to the AMF (250 A m^{-1}, 245 kHz), the LM droplet floated in the water and maintained its position over the coil center despite the glass tube being reciprocating vertically (Figure 2E and Video S4). In addition to being attributable to the repulsive force generated by eddy currents, such a stable electromagnetic levitation behavior is attributable to the Brownian motion of water molecules surrounding the LM, which can prevent horizontal deviation of its position, thus maintaining the orientation of the repulsive force overcoming the gravity of the LM.

AMF-Mediated Exothermic Properties of LMs

Hyperthermia therapy is a type of cancerous tumor treatment in which the body tissue is exposed to high temperatures (Pang, 2015). Numerous challenges must be overcome before hyperthermia can be considered a standard treatment for cancer. Many clinical trials evaluating the effectiveness of hyperthermia are underway. Research into hyperthermia, in combination with other therapies, for the treatment of different cancers as well as improvements in existing hyperthermia techniques are urgently required. Thus we first

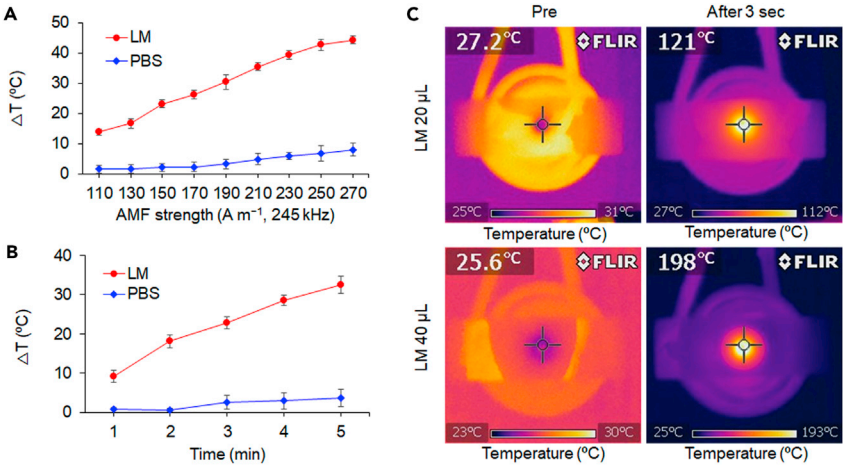

Figure 3. AMF-Mediated Exothermicity of an LM Blob

(A) AMF-strength-dependent heating curves of the LM (25 μL, round) and PBS (25 μL, diamond) in water (5 mL). AMF duration: 3 min. Data are represented as mean ± SEM.

(B) Time-dependent heating curves of the LM (25 μL, round) and PBS (25 μL, diamond) in water (5 mL). AMF strength: 150 A m^{-1}, 245 kHz. Data are represented as mean ± SEM.

(C) Thermal images of the LM in air before and after application of the AMF (250 A m^{-1}, 245 kHz) for 3 s.

investigated the AMF-induced potency of LMs as an effective hyperthermia technology and explored the magnetic properties of the LMs.

The AMFs used for heat dissipation experiments were generated from a flat spiral coil connected to an AC-current-tunable system (frequency fixed at 245 kHz) to vary the AMF strength. A glass vial containing 25 μL of LM and 5 mL of water was positioned above the center of the coil. As illustrated in Figure 3A, the LM increased the temperature of the solution linearly when an AMF was applied for 3 min in the *H*-field range from 110 to 270 A m^{-1}. The difference in temperature (ΔT) reached approximately 45°C at the maximum AMF strength (H = 270 A m^{-1}), whereas the same volume of phosphate-buffered saline (PBS) used as a control showed only a negligible increase (ca. 8°C). In another experiment, the AMF strength was fixed at H = 150 A m^{-1} for observation of the time-dependent heat generation properties of the LM. The change in ambient temperature of the LM increased with increasing AMF exposure and reached 32°C after 5 min (Figure 3B). To directly evaluate the LM surface temperature under the AMF, we deposited LM onto a glass slide and placed it on the coil in air. After only 3 s of exposure to the AMF (H = 250 A m^{-1}), the temperatures of 20 μL and 40 μL of LM surprisingly increased to 121°C and 198°C, respectively (Figure 3C).

Effect of the oxide skin of the LM droplet on the increase in temperature was also investigated (Figure S4A). The difference of temperature elevation of two LM blobs was compared in the presence or absence of 0.1 N HCl, which can prevent oxide generation on the LM surface (Lu et al., 2015; Yamaguchi et al., 2015). After the result, the oxide skin layer of LM has no effect on the AMF-induced LM exothermicity probably because of its ultrathinness (~1 nm) (Chiechi et al., 2008; Larsen et al., 2009).

The AMF-thermal conversion efficiency of the LM blob in Milli-Q (MQ) water was about 86.3%, although the efficiency was gradually decreased over time probably due to the power losses of the instrument by the strong AMF induction (Figure S4B and see Transparent Methods for more details). Anyway, these results demonstrate that the LM possesses excellent electromagnetic induction heating characteristics and that the amount of heat generated is readily controllable by adjusting the AMF strength, the exposure duration, and the LM volume.

In Vitro Cancer Elimination by AMF-Induced LM

Encouraged by the promising electromagnetic heating efficiency, we next evaluated the cytotoxicity and *in vitro* magnetic hyperthermia efficacy of LM using various cancer cell lines. A549 (lung carcinoma), U2OS (osteosarcoma), and HT-29 (colorectal adenocarcinoma) were first seeded in 12-well plates at 70% confluence with 1 mL medium. An LM blob (40 μL) was added to the wells and subsequently exposed to an AMF

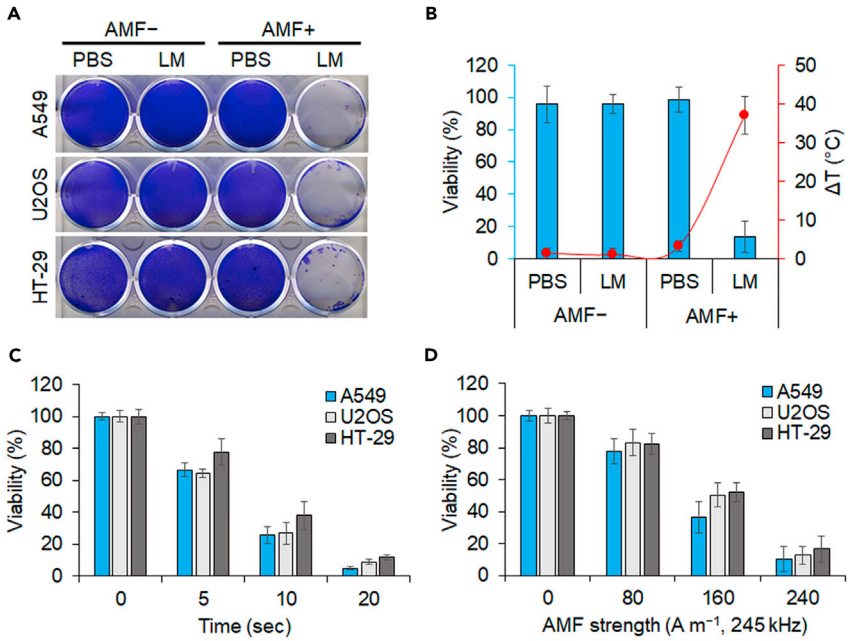

Figure 4. *In Vitro* Cancer Elimination by AMF-Induced LM Blob

(A) Crystal violet staining of cells incubated with LM or PBS following AMF treatment. The LM (40 μL) was incubated with cells in medium (1 mL) and heated under an AMF (200 A m^{-1}, 245 kHz) for 3 min. Staining was performed 24 hr post treatment.

(B) AMF-induced elimination of cancer cells (HT-29) by heat generation. LM (20 μL) and PBS were incubated with HT-29 in medium (500 μL) and exposed to an AMF (200 A m^{-1}, 245 kHz) for 3 min. The corresponding temperature change is represented by the orange curve. Data are represented as mean ± SEM.

(C) Time-dependent change in viability of cancer cell lines treated with LM (20 μL) in medium (200 μL) under an AMF (200 A m^{-1}, 245 kHz). Data are represented as mean ± SEM.

(D) AMF strength-dependent change in viability of cancer cell lines treated with LM (20 μL) in medium (200 μL) over a period of 10 s. Data are represented as mean ± SEM.

(H = 200 A m^{-1}) for 3 min. The treated cells together with the LM were then cultured for 24 hr, and the cell viability was tested by crystal violet staining. As illustrated in Figure 4A, in the absence of the AMF, neither the LM-treated group nor the PBS control group showed any decrease in cell viability, indicating that the LM alone is less toxic. By contrast, almost all the cells incubated with the LM and then exposed to the AMF were killed. To obtain quantitative results, we conducted the same experiments using a Cell Counting Kit-8 (CCK-8 kit) and measured the temperature change. Likewise, LM without the AMF did not affect the viability. However, the viability of HT-29 cells incubated with LM decreased to 14% compared with the viability of cells in the PBS control and the temperature (20 μL of LM in 500 μL of medium) increased by 37°C simultaneously under the applied AMF (H = 200 A m^{-1}) (Figure 4B).

We next examined the cancer cell elimination effect of LM immediately after AMF treatment without an additional culture period. The magnetic hyperthermia efficacy of the LM was dependent on the AMF treatment time and strength (Figures 4C and 4D). Notably, most of the cancer cells were killed within only 10–20 s under the AMF with field strength in the range 200 ≤ H ≤ 240 A m^{-1}. This more effective performance is attributed to the small volume of the medium (20 μL of LM in 200 μL of medium) used in this case during AMF heating. Together with the results of the viability tests, these evidences imply that LM is efficient and useful for cancer cell magnetic hyperthermia.

In Vivo Magnetic Thermotherapy with LMs

The next step consisted of assessing the heating effect of the LM *in vivo* on nude mice bearing solid tumors. The biggest advantage of LM for biological applications when compared with other functional materials, such as magnetic nanoparticles, is that LMs can be easily handled as injectable liquids without chemical modifications or complicated multistep processes. Herein, we took advantage of this useful

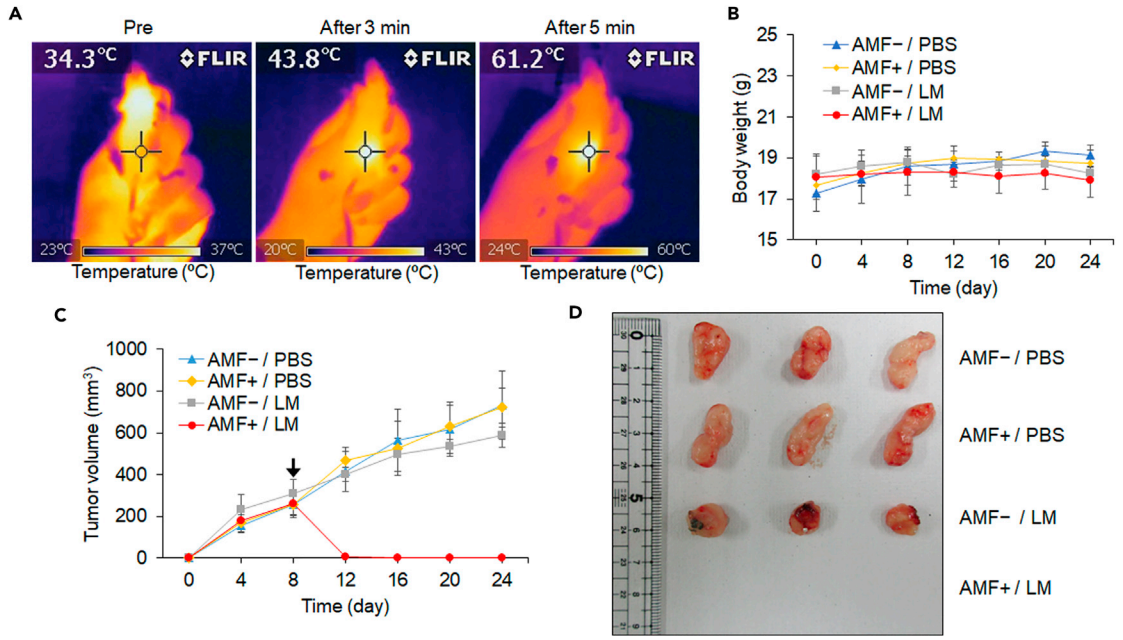

Figure 5. *In Vivo* Cancer Treatment by an AMF-Driven LM Blob

(A) Thermal images of HT-29 tumor-bearing mice after intratumoral injection of the LM (30 μL) under a continuous period of AMF treatment (150 A m^{-1}, 245 kHz).

(B) Body weight of mice in different groups. Data are represented as mean ± SEM.

(C) Growth curve of tumors in mice from different groups. The LM injection and AMF treatment were performed at 8 days (black arrow) post-transplantation of HT-29 cancer cells. Data are represented as mean ± SEM.

(D) Representative photograph of the tumor tissue collected from mice in different groups 16 days post AMF treatment.

attribute of the soft and flexible liquid state of the LMs and our finding of AMF-driven LM exothermicity for *in vivo* tests. When the tumor volumes reached approximately 250 mm^3, mice were randomly divided into four groups (n = 5): PBS injection only (AMF−/PBS), PBS injection and AMF exposure (AMF+/PBS), LM injection only (AMF−/LM), and LM injection and AMF exposure (AMF+/LM). Mice were intratumorally injected with 30 μL of LM or PBS and subsequently subjected or not subjected to an AMF (150 A m^{-1}, 245 kHz) for 5 min. The temperatures of the tumors and mice were monitored with an infrared camera at different time intervals (Figure 5A). The tumor injected with LM underwent local heating under the applied AMF, where the temperature increased to 43.8°C (9°C increase) after 3 min and to 61.2°C (27°C increase) after 5 min. The tumor volumes and body weights of each group of mice were recorded for 16 days after treatment (Figures 5B and 5C). The tumors from all the control groups (AMF−/PBS, AMF+/PBS, and AMF−/LM) increased in size, whereas the LM-injected tumors were completely eliminated by AMF heating (Figures 5C and S5A). Notably, the treated mice from the AMF+/LM group did not exhibit tumor recurrence or loss of body weight at the end of the experiment (Figures 5B–5D). Interestingly, a slight tumor regression was observed in the group of mice injected with LM but not subjected to AMF exposure (Figures 4B and 4C). Indeed, we observed that the tumor blood vessels were occupied by the LM after injection, as shown in Figure S5B, suggesting that such inhibition might arise from the LM obstructing the tumor capillaries and preventing nutrient absorption (Avery et al., 2016; Chechetka et al., 2017).

We also observed how LMs behave during AMF induction under a skin using an *ex vivo* model that is made of a pig skin and two glass slides (Figure S6 and Video S5). Interestingly, the LM could be dramatically transformed by AMF-induced manipulation in small spaces under the skin, although most of the LM still remained in the *ex vivo* model. The LM transformations might be potentially used for their comprehensive heating and effective elimination of cancer cells. In addition, the LM could be directly removed from the injected part using this AMF-applied diverse LM motion after cancer hyperthermia, and could simultaneously effectively eliminate cancer at the target site during its movement. Anyway, we are sure that the exothermic behavior of the AMF-driven LM substantially allows effective *in vivo* cancer elimination as a flexible heat generator in physiological environments and biological systems.

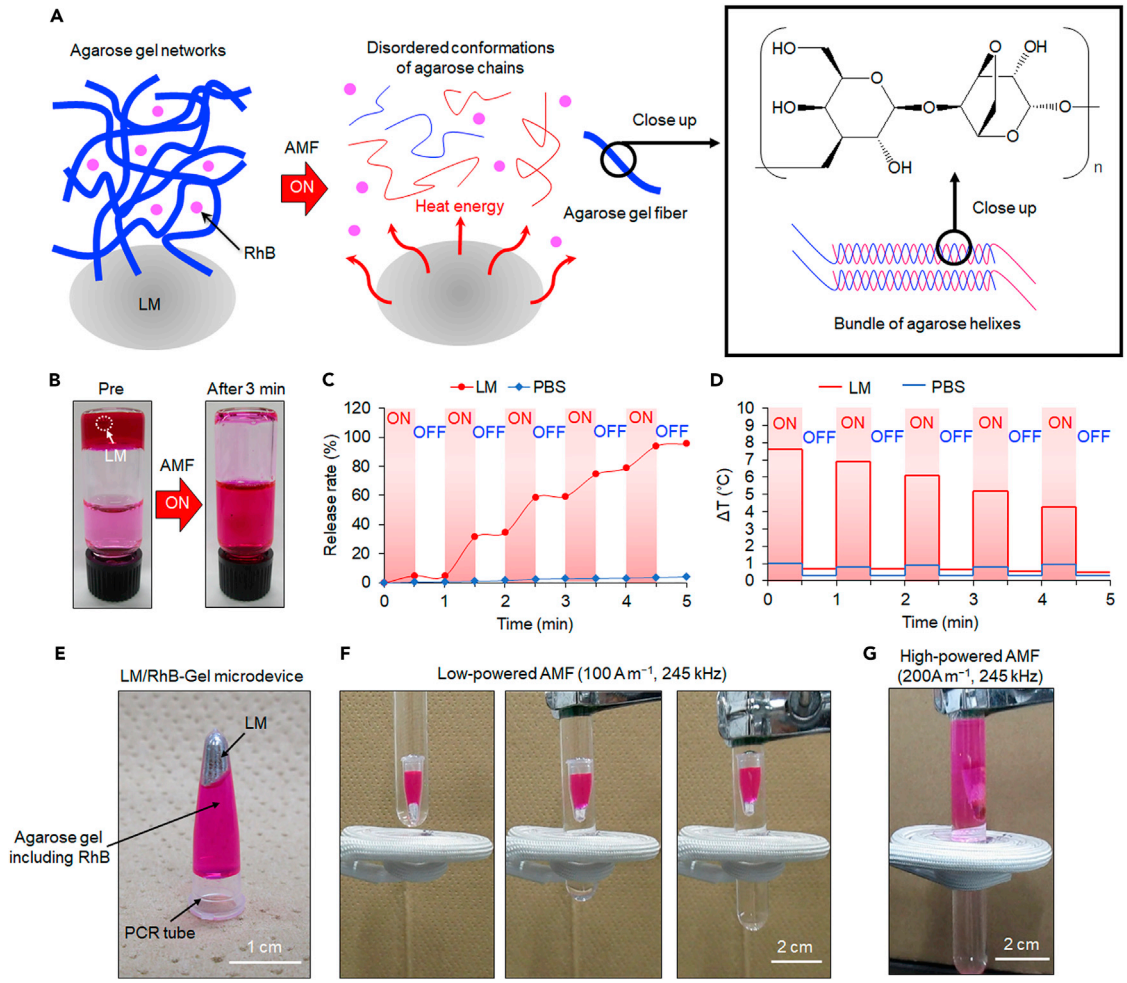

Figure 6. AMF-Controlled Spatiotemporal Drug Release from an LM-Hydrogel Microdevice

(A) Schematic illustration of gel-sol transition of LM-agarose gel composite upon AMF induction.

(B) 1 mL hydrogel matrix (agarose, 2% w w^{-1}; RhB, 0.5 mg mL^{-1}) containing LM (20 μL) in addition with 2 mL water before and after AMF (200 A m^{-1}, 245 kHz) exposure for 3 min.

(C and D) AMF-modulated release profile (C) and temperature change (D) of LM- or PBS-containing hydrogel matrix over the period of time. The "ON" stage indicates exposure to the AMF (200 A m^{-1}, 245 kHz), whereas the "OFF" stage indicates absence of the AMF.

(E) Depiction of the LM/RhB-Gel microdevice consisting of LM (20 μL), agarose (2%, w w^{-1}, 200 μL), RhB (0.5 mg mL^{-1}), and a PCR tube.

(F) Sequential snapshots of LM/RhB-Gel microdevice electromagnetic levitation induced by low-powered AMF (100 A m^{-1}, 245 kHz).

(G) Photograph of the LM/RhB-Gel microdevice electromagnetic levitation and RhB release behavior induced by high-powered AMF (200 A m^{-1}, 245 kHz).

AMF-Controlled Spatiotemporal Drug Release from LM Microdevice

Our final goal of the current study is to achieve remote control of an LM medical device in physiological environments for various therapeutic bioengineering purposes, particularly for cancer therapy, using the electromagnetic properties of LMs. Because of the thermal and motion capabilities rendered by an AMF, we applied the promising toxicity profile of an LM to a drug delivery system that enables controlled release of the carried therapeutic molecules at a desired location. As illustrated in Figure 6A, the LM (20 μL)-containing hydrogel depot was fabricated using 1 mL low-melting-point (≤45°C) agarose (2%, w w^{-1}) and rhodamine B (RhB, 0.5 mg mL^{-1}). Figure 6A shows our concept for the AMF-induced gel-sol transition of LM-agarose gel composites. Agarose gel is one of the most popular thermo-reversible hydrogels. In hot solutions, agarose chains exist in a stiff and disordered conformation. Upon cooling below 40°C, the chains settle into helices that subsequently aggregate into bundles (Aymard et al., 2001); however, the mechanism of such structural changes during the phase transition is not well understood. Here, an LM droplet was mixed at 50°C with the agarose aqueous solution and RhB was subsequently loaded as a drug model,

followed by rapid cooling to form the hydrogel matrix. MQ water (2 mL) was added onto the solidified matrix and subsequently exposed to an AMF to study the thermal effect of the embedded LM on the release of RhB. After AMF exposure (200 A m^{-1}, 245 kHz) for 3 min, the LM had almost thawed the whole hydrogel, leading to the complete release of RhB into the additional 2 mL water (Figure 6B).

The same system was also used to investigate the controllability of drug release by ON-OFF cycling (30 s ON, 30 s OFF) of the AMF. As depicted in Figures 6C and 6D, in the absence of the LM, the difference in the release rate and temperature between the ON and OFF states was negligible. By contrast, under the influence of the AMF (state "ON"), the LM/hydrogel matrix exhibited a dramatic increase in temperature, with a concomitant increase in the release rate of RhB. However, when the AMF was turned OFF, the temperature change returned to ca. 0.7°C, thus barely affecting RhB release. This behavior was reproducible over five continuous ON-OFF cycles of AMF exposure (150 s ON, 150 s OFF), eventually achieving a 100% release rate. Notably, over time, the LM-induced temperature difference (ΔT) achieved during each ON-OFF cycle tended to decrease, which is also reflected in the reduction of the slope of the release rate curve associated with the AMF ON state. This trend is attributed to the transformation of the agarose gel to water, which has a greater specific heat capacity than the agarose gel.

To achieve the spatiotemporal targeted drug release using the LM/hydrogel system, we developed a more facile LM/RhB-Gel pill-shaped microdevice, where LM (20 μL), agarose (2%, w w^{-1}, 200 μL), and RhB (0.5 mg mL^{-1}) were entirely packaged in a small polymerase chain reaction (PCR) microtube (ca. 2000 μm in length and 500 μm in width) (Figure 6E). Because of the electromagnetic levitation effect of the LM, the LM/RhB-Gel microdevice was dynamically suspended in water under an AMF (Figure 6F and Video S6). The position of the microdevice relative to its loading container could be adjusted by shifting either the AMF coil or the container. Notably, the low-powered AMF (100 A m^{-1}, 245 kHz) impelling the microdevice did not trigger any diffusion of RhB (as indicated by a lack of red color in the water) during the movement. When the suspension behavior was maintained as the AMF H-field was increased to 200 A m^{-1}, the LM gradually melted the surrounding agarose gel and expanded the air inside, eventually leading to a massive local release of RhB (Figure 6G). We have also confirmed RhB-releasing behavior from the improved microdevice once per day over 3 days with and without AMF application (Figure S7).

To further confirm the thermal effect on drug release from the LM/RhB-Gel microdevice, we immersed the microdevice in 5 mL water and examined both the RhB content in the water and the temperature change under weak (100 A m^{-1}, 245 kHz, for movement) or strong (200 A m^{-1}, 245 kHz, for release) AMFs. As shown in Figures S8A–S8C, within 3 min, the weak AMF only induced a slight elevation of temperature and a slight release of RhB into the water, indicating little loss of RhB during microdevice movement. By contrast, a substantial increase in RhB concentration was observed in the case of high-powered AMF exposure (Figure S8B). Collectively, these results demonstrated that, with manipulation of the AMF strength, the designed LM/RhB-Gel microdevice could effectively release RhB to a targeted site in a water environment in which the temperature is barely affected during the microdevice transportation step.

With respect to future clinical utilization, assessments of the biosafety of the versatile LM/Gel microdevice and its thermal effect during transportation are critical. Given that agarose gel is recognized as a safe material, we examined the long-term reaction of nude mice administered LM (2 mg) by either oral feeding or intraperitoneal injection. As we expected, none of the mice administered LM showed a loss of body weight within 24 days (Figure S8D). The *in vitro* cell viability was assessed using normal human fibroblast cells (TIG-3). Cells grown in 3 mL culture medium were exposed to a low-powered AMF (100 A m^{-1}, 245 kHz) in addition to the LM/Gel microdevice. As shown in Figure S8E, after 2 min of exposure, the microdevice did not affect cell viability immediately or 48 hr post treatment. We also confirmed that LM is less toxic in mice after subcutaneous injection, as demonstrated by various biocompatibility analyses, including blood investigations and X-ray computed tomographic (CT) scanning (Figure S9 and Table S1). The volume of injected LMs for subcutaneous administrations was 30 μL. Careful observations revealed no mice death with subcutaneous LM injections (Figure S9 and Table S1). In addition, complete blood cell count (CBC) and biochemical examinations of LM were all normal, at least for 28 days with both routes of administration (Table S1). In particular, virtually no changes in the levels of inflammatory markers (i.e., white blood cell [WBC] and C-reactive protein [CRP]) were seen after subcutaneous injections of LM. Furthermore, we studied the distribution of LM after its subcutaneous injection into the back position by X-ray CT (Figure S9 and Video S7). It is known that the strong X-ray attenuation property and the high

density of LM are effective for *ex vivo* and *in vivo* X-ray imaging (Wang et al., 2014; Chechetka et al., 2017). As a result, the injected LM could remain safely in the back of mice without toxic side effects for at least 7 days. Meanwhile, our final goal of this research is to build a functional drug delivery microdevice of LM via oral administration. Herein, the X-ray CT imaging of mice and their feces has been complementarily performed for 24 hr after oral feeding of LM to clarify the ways of excretion of LM for this future big vision. LM was apparently excreted as feces over time from the body of the mice (Figure S10A). In fact, LM was not accumulated at all in the liver, although a very small amount of LM (small bright spots) was observed in the pyloric region of stomach, small intestine, and cecum after its oral administration for 6 hr (Figure S10B). The X-ray bright spots derived from LMs completely disappeared after oral feeding for 24 hr (Figure S10B). These *in vitro* and *in vivo* results indicate that the LM/Gel microdevice can potentially remotely deliver therapeutics without any side effects in a physiological environment.

We believe that various electromagnetic performances of an LM/Gel microdevice are potentially effective for remote controlling of the microdevices particularly in parts of the digestive system, such as the gullet, stomach, small intestine, and colon, as an advanced drug delivery system, in addition to the above-mentioned use of LMs in cancer elimination (Figure S11). High controllability of the mobility of an AMF-induced LM/Gel microdevice was successfully achieved in a plastic test tube (ca. 20 mm in diameter), which is a simple model of the digestive organs (Figure S11A). Indeed, an LM/Gel microdevice could smoothly move in a space containing PBS buffer without any stacking (Figure S11B). These results showed that the AMF induction was sufficient to drive the magnetic characteristic of the LM/Gel microdevice under physiological conditions, thereby allowing it to easily move through a space.

DISCUSSION

In this study, we described the design and application of AMF-induced LM manipulations. Locomotion, electromagnetic levitation, and transformations of LM blobs, which are critical capabilities for the development of intelligent materials, could also be spatiotemporally controlled using wireless AMF applications. These high mobilities of AMF-driven LM manipulations would not only expand the concept of LMs but also provide a sophisticated movement mechanism that enables smooth, high-speed, and fine operations. At a minimum, the current three-dimensional motions of LM blobs driven by applied AMFs surpass the capabilities of ordinary LM manipulation methods (Tsai et al., 2009; Sheng et al., 2014; Eaker and Dickey, 2016; Gough et al., 2016) involving electrical and oxidation-reduction reactions, which are limited to horizontal two-axis directional movements. Although electromagnetic levitation of conductive solid metals has been already reported, we believe that the unique and natural advantages of EGaIn in substantial terms of softness, flexibility, and workability in addition to the electromagnetic dynamicity allow contributing toward the creation of diverse potential applications. We are also sure that wettability of oxide layer in a self-limiting reaction is important for AMF-driven LM mobility on substrates and affinity of LMs for various biological interfaces. Indeed, the presence of the oxide layer increases the adhesion of the LMs onto oxygen-containing inorganic and organic substrates via weak but surface-dispersed van der Waals forces (Carey et al., 2017).

Upon AMF induction, the LM droplets were rapidly heated via an eddy current. The heating capacity of an electrically conductive material is related to eddy currents generated by electromagnetic induction; these eddy currents lead to Joule heating (Haimbaugh, 2015). The favorable electrical conductivity (3.46×10^6 S m^{-1}) of LM (Karcher et al., 2003) enables the AMF to induce an eddy current passing through the LM and thus produce substantial heat. On the basis of the skin effect, eddy current heating is strongly associated with the size and geometry of the conductor (Boekelheide et al., 2006). Therefore if the resistivity of the LM is assumed to be constant, then a larger volume of LM exhibiting a greater surface area is reasonably expected to provide better heat generation performance (Figure 3C). Notably, conventional nanoparticles used for magnetic hyperthermia required a high-powered AMF with a typical amplitude and frequency (*Hf*) on the order of 10^9 Am^{-1} s^{-1} (Shubitidze et al., 2015). Moreover, an *Hf* factor greater than 5×10^9 Am^{-1} s^{-1} is potentially harmful for patients (Hergt and Dutz, 2007). By contrast, LM demonstrates excellent heat generation performance with an *Hf* factor on the order of 10^7 Am^{-1} s^{-1}, which is two orders of magnitude smaller than that needed for magnetic nanoparticles. Meanwhile, the maximum magnetic field strength of our system (270 A m^{-1}) is about 10,000-fold lower than those used for conventional magnetic resonance imaging (MRI) (239×10^4 A m^{-1}) (Tayari et al., 2017). We believe that the magnetic field strength of our system may not be a crucial issue for local fields just by being careful to apply them away from sensitive areas. Thus from the viewpoint of energy consumption and safety of the AMF, LM is a promising material for magnetic hyperthermia

technology. Indeed, our results also show that LMs under an applied AMF can be used to effectively eliminate *in vitro* and *in vivo* cancer cells because of their powerful exothermicity.

Near-infrared (NIR) light, radio frequency (RF), microwave (MW), ultrasound (US), and AMF are the most commonly used technological platforms for cancer hyperthermia. The maximum penetration depth of NIR light in a biological tissue is of the order of a few millimeters, making this approach quite inefficient for the treatment of deep tumors (O'Neal et al., 2004; Stafford et al., 2011). RF ablation also presents important limitations owing to its poor depth penetration, resulting in severe invasiveness and incomplete tumor destruction (Curley, 2003; Arciero and Sigurdson, 2008). The penetration of MW in biological tissues is also very poor (Vogl et al., 2017). Moreover, the focal spot generated by MW is unsatisfactory at the normal-cancerous tissue interface because of the long wavelength of the MW. US can achieve much better penetration depths than MW (Diederich and Hynynen, 1999). However, because its acoustic wavelength is very short, the focal spot generated by US is very small (millimeter or submillimeter in diameter) compared to a large tumor (centimeters in diameter on the average). Thus many focal spots are required for complete tumor coverage, which results in long treatment and missed cancer cells. With AMF approach there are no limitations to the penetration depth (Bulte and Kraitchman, 2004; Laurent et al., 2010; Pankhurst et al., 2009). We confirmed that AMF certainly penetrated thick pig skins (at least 3 cm) to effectively generate thermal energy from the LM droplet by the simple AMF laboratory instrument (Figure S12). Herein, we believe that AMF-driven LM hyperthermia would overcome the problem of traditional treatments.

Two techniques are currently used to deliver the nanoparticles to the tumor for hyperthermia. The first is to deliver particles to the tumor vasculature (Matsuki and Yanada, 1994) through its supplying artery; however, this method is not effective for poorly perfused tumors. Furthermore, for a tumor with an irregular shape, inadequate nanoparticle distribution may cause under-dosage of heating in the tumor or overheating of the normal tissue. The second approach is to directly inject nanoparticles into the extracellular space in the tumors (Salloum et al., 2008). The nanoparticles diffuse inside the tissue after injection of the nanofluid. However, nanoparticles tend to easily disappear from the target site after injection owing to their small particle size. As a result, nanoparticles lose their effective heating property. It means that repeated heating of nanoparticles is not available for long duration, although surviving cancer cells are often regenerated at the same position. Eventually, nanoparticles should be injected each time there is cancer recurrence. This is disadvantageous in terms of the quality of a patient's life. LM could be implanted on a long-term basis for cancer hyperthermia in a similar way as solid metal-based implant materials and devices (e.g., artificial bone and pacemaker). In fact, gallium-based LMs worked as implantable teeth materials with high biocompatibility (Kaga et al., 1996; Dunne and Abraham, 2000). Anyway, owing to the fluidity of LM, a tumor with an irregular shape can be sufficiently covered by introducing LM in a proper manner. In addition, repetitive exothermic behavior from AMF-induced LM might be useful for cancer eradication to prevent cancer recurrence and metastasis in future practical situations.

Ordinary ferrofluids composed of magnetic nanoparticles have the advantages of nanosized effects, such as heat homogeneity and tumor-specific accumulation ability. However, AMF-induced exothermic behavior of a commercially available ferrofluid was less than that of the LM system (Figure S13). In addition, ferrofluid easily dries up just after incubation for only an overnight even at ambient temperature and is then transformed to a hard-state solid material that is inconvenient to handle (Figure S14A). LMs are highly stable and can keep in liquid state for long period at normal temperature because of their non-volatility.

Meanwhile, it is well known that gold and silver nanoparticles are unstable to heating and freezing owing to the shape deformations (degradation) (Albert et al., 2009; Zou et al., 2010). In addition, these metal nanoparticles do not have high dispersing stability in aqueous solution, including salts such as buffers and cell culture media (Capek and Tiwari, 2015). Furthermore, heat generation from these metal nanoparticles basically requires relatively higher frequency (mainly 13.56 MHz) AMF that has low biological permeability (Abadeer and Murphy, 2016). LMs have very high thermal stability. Indeed, LM blobs were obviously stable even after repetitive heating in salt solution by AMF application (Figure S14B). The exothermic ability of LMs is also driven by low-frequency AMF (245 kHz) that can deeply penetrate into the body (Young et al., 1980; Chen et al., 2015).

The nanodimensional properties of magnetic nanoparticles can potentially lead to toxic side effects at the molecular level, such as inflammation, impaired mitochondrial function, and gene damage (Hussain et al., 2005; Sadghiani et al., 2005; Ankamwar et al., 2010; Singh et al., 2010), during their applications in

physiological environments. From these perspectives, LMs for the possible treatment of malignant epithelial tumors have become an area of interest because they can be manipulated as a bulk material. Nevertheless, ligand (e.g., antibody and peptide)-functionalized LM nano/micro particles are also emerging as promising agents for future targeted cancer therapy (Lu et al., 2015; Chechetka et al., 2017). However, LM nano/micro particles do not have strong exothermicity by AMF application compared with LM blobs regardless of the presence or absence of chemical functionalization with poly(ethylene glycol) methyl ether thiol (PEGMET) probably due to their low electromagnetic property associated with size effect (Figure S15). We are, thus, currently improving the efficacy and selectivity of an AMF-induced LM nano/micro particle technology by investigating on the unique shape and optimal size of the particles for effective and targeted cancer elimination. Meanwhile, the dynamic behavior of these LM nano/micro particles cannot be controlled at all by AMF application because the size effect of LM is also strongly affected on manipulation (Figure S16). We are currently exploring the optimal size of LM droplets for applying the AMF-driven technology in medical devices on chips (Guan et al., 2017).

Although conventional ferrofluids are also controllable by AMF application for remote manipulation as well as the current AMF-induced LM system, the mobilities of an AMF-induced ferrofluid are quite insufficient compared with our LM system in physiological environment (Figure S17 and Video S8). Twenty microliters of ferrofluid (sodium tetradecene sulfonate-modified magnetite nanoparticles-distilled water suspension, ca. 35 wt% in concentration and ca. 10 nm in diameter) was loaded into a spindle-shaped glass tube that was prefilled with 3 mL water. After concentrating ferrofluids to the bottom by centrifugation, the glass tube was horizontally placed and we approached the glass tube onto the coil center at a constant speed. Along with the tube shifting, LM was keeping its integrity and position steady as expected. However, although dense ferrofluids were attracted by AMF, a large amount of them were left behind. Indeed, ferrofluid is rapidly diffused and dispersed in aqueous solution. After all, their mobilities are not controllable at all by AMF induction. We also investigated the AMF-controlled motion of diluted ferrofluids (5 μL in 3 mL water, simple spin-down), which is much more similar to physiological condition. The diluted ferrofluids did not show any relative movement at all in the glass tube, indicating that ferrofluids may not be controllable by AMF when the magnetic particles are tenuous. Taken together, AMF-induced LM clearly represents high controllability in physiological conditions. In addition, high biocompatibility and non-volatility of LM are advantages over conventional ferrofluids, which are basically prepared by toxic surfactants and volatile solvents.

Furthermore, the pill-shaped microdevice based on LM and agarose hydrogel composites is remotely levitated and releases drug molecules in a controlled manner under an applied AMF. This study is the first to exploit the powerful electromagnetic properties of LMs for eradication of cancer cells, achieving basic motion and melting drugs containing hydrogels. The findings described herein provide a valuable therapeutic bioengineering and related biotechnology with potential applications in various scientific fields, including cancer research and electromagnetic materials science. We believe the dramatic morphological changes of LM triggered by AMF induction could also be useful in the development and design of magnetostrictive materials (Clark and Belson, 1972; Clark et al., 2000) and extreme-environment actuators (Swallow et al., 2017). The strategy used in this study addresses several fundamental issues related to the fabrication of biocompatible microdevices. The entire LM consists of low-toxicity EGaIn, and its performance is driven by simple electromagnetic mechanisms. LM itself can also be easily removed from the biological system after operations, when it is packed in a pill-shaped microdevice, to prevent accidents from other magnetic fields. In addition, we expect that the manipulation capabilities of the LM system are effectively controlled in the stomach and intestines because there are huge spaces for controlling the movement of LMs. These AMFs controlled the wireless dynamics of a pill-shaped microdevice and triggered the spatiotemporal drug release, which could be also useful as oral and intrarectal drug delivery systems for future cancer elimination. The electromagnetic hyperthermia of LMs could be also utilized in combination with chemotherapy to improve cancer cell elimination in the stomach and intestines, since hyperthermia can render tumor cells temporarily more sensitive to the synergetic damaging effects of chemotherapeutics. This work is a proof-of-principle study demonstrating that *in vitro* operations of LM devices can be mediated by AMF induction. Further studies are needed to investigate *in vivo* manipulation systems and appropriate design of devices and construction of suitable animal models to determine the effective performance of an LM device in a deep digestive organ for advanced drug delivery systems.

Previous works on drug delivery microdevices have been focused mainly on the sustained release of a single compound whose release profile must be determined; in addition, these microdevices usually

have complicated and invasive mechanisms for triggering delivery (Yoo et al., 2011; Timko et al., 2014). The three-dimensional spatial position of the LM pill-shaped microdevice can be accurately controlled and triggered to release drug molecules. Given these capabilities, our microdevice could find applications in advanced drug delivery and other applications that require control of microenvironments around cancerous tumors and could bring the field one step closer to the development of functional materials that can safely interact with humans and other living systems.

Although research groups have reported functional ferrogels—the use of a uniform magnetic field for directionally controlled drug releasing—we find that ordinary ferrogels are inferior in size effect (Liu et al., 2015). In general, the magnetic responses of composites are dramatically decreased when they have large thickness. In other words, conventional ferrogels cannot be prepared in fixed shapes like a thin membrane. In addition, it is necessary to construct an optimal magnetic field distribution system for sufficient magnetic responsibility to release drug molecules. Furthermore, the materials must be carefully designed for complicated interfacial affinity between the magnetic nanoparticle and the gel matrix owing to the low dispersibility of magnetic nanoparticles in matrixes. In light of this fact, it has been demonstrated that various shapes of composites such as cylindrical and pill-shaped devices can be easily prepared, control release of RhB is achieved by simple AMF irradiation without consideration of complicated magnetic field distribution system; oxidized skin layer of LM allows improving the interfacial affinity at the interface of the LM and hydrogel matrix.

The attractive properties of LMs such as fluidity may also render them better suited to some applications of the drug delivery system than other electromagneto-responsive gels such as hybrid gel encapsulating aluminum cramps. The fluidity of LM might be useful to prepare a pill-shaped microdevice indeed because LM can be conveniently handled as a liquid using simple pipetting technique for filling into a device. The fluidity of LM can also possibly seem to be causing physical damages on a biological tissue when the LM accidently comes out from the device during heating. Meanwhile, electromagnetic solid materials like aluminum require fabrication (cutting, molding and filling, etc.) for making a microdevice. Hardness and robustness of solid aluminum also possibly lead to harmful physical sticking onto the tissues. At least, we confirmed low heat generation of aluminum clumps by AMF induction (Figure S13). Indeed, the AMF-induced exothermic property of aluminum clumps was lower than that of the LM system under the same conditions. Furthermore, we believe that fluidity of LM is also an important factor in both cancer thermotherapy and drug delivery devices because it contributes to injectability and effective heating process. For cancer hyperthermia, fluidity of LM is able to effectively heat the entire target region that is comprehensively enclosed by injection of LM. On the other hand, patterning and multi-heating points are easily designed in the LM/agarose gel composite for AMF-induced acceleration of decomposition speed of gel matrix (Figure S18). Taken together, we are sure that the AMF-driven LM system has fruitful advantages to build up smart microdevices, particularly in terms of fluidity that can be convenient handled and powerful exothermic property for the potential use to develop innovative therapeutic bioengineering.

METHODS

All methods can be found in the accompanying Transparent Methods supplemental file.

SUPPLEMENTAL INFORMATION

Supplemental Information includes Transparent Methods, 18 figures, 1 table, and 8 videos and can be found with this article online at https://doi.org/10.1016/j.isci.2018.04.012.

ACKNOWLEDGMENTS

This work was supported by a Japan Society for the Promotion of Science (JSPS) KAKENHI Grant-in-Aid for Scientific Research (B) (16H03834), a JSPS KAKENHI Grant-in-Aid for Challenging Exploratory Research (16K13632), and a JSPS KAKENHI Fund for the Promotion of Joint International Research (Fostering Joint International Research) (16KK0117).

AUTHOR CONTRIBUTIONS

E.M. conceived and designed the experiments; Y.Y. performed the experiments; Y.Y. and E.M. analyzed the data; and E.M. prepared the manuscript. Both authors discussed the results and contributed to writing the manuscript.

DECLARATION OF INTERESTS

The authors declare no competing interests.

Received: February 26, 2018
Revised: March 27, 2018
Accepted: April 6, 2018
Published: May 25, 2018

REFERENCES

Abadeer, N.S., and Murphy, C.J. (2016). Recent progress in cancer thermal therapy using gold nanoparticles. J. Phys. Chem. C *120*, 4691–4716.

Albert, G.C., Roumeliotis, M., and Carson, J.J.L. (2009). The effect of temperature and freeze-thaw processes on gold nanorods. Nanotechnology *20*, 505502.

Arciero, C.A., and Sigurdson, E.R. (2008). Diagnosis and treatment of metastatic disease to the liver. Semin. Oncol. *35*, 147–159.

Avery, R.K., Albadawi, H., Akbari, M., Zhang, Y.S., Duggan, M.J., Sahani, D.V., Olsen, B.D., Khademhosseini, A., and Oklu, R. (2016). An injectable shear-thinning biomaterial for endovascular embolization. Sci. Transl. Med. *8*, 365ra156.

Aymard, P., Martin, D.R., Plucknett, K., Foster, T.J., Clark, A.H., and Norton, I.T. (2001). Influence of thermal history on the structural and mechanical properties of agarose gels. Biopolymers *59*, 131–144.

Ankamwar, B., Lai, T.C., Huang, J.H., Liu, R.S., Hsiao, M., Chen, C.H., and Hwu, Y.K. (2010). Biocompatibility of Fe_3O_4 nanoparticles evaluated by *in vitro* cytotoxicity assays using normal, glia and breast cancer cells. Nanotechnology *21*, 075102.

Boekelheide, Z., Hussein, Z.A., and Hartzell, S. (2006). Electronic measurements in an alternating magnetic field for studying magnetic nanoparticle hyperthermia: minimizing eddy current heating. IEEE Trans. Magn. *52*, 5400304.

Bulte, J.W., and Kraitchman, D.L. (2004). Iron oxide MR contrast agents for molecular and cellular imaging. NMR Biomed. *17*, 484–499.

Capek, I., and Tiwari, A. (2015). DNA Engineered Noble Metal Nanoparticles: Fundamentals and State-of-the-art of Nanobiotechnology (Wiley-VCH).

Carey, B.J., Ou, J.Z., Clark, R.M., Berean, K.J., Zavabeti, A., Chesman, A.S.R., Russo, S.P., Lau, D.W.M., Xu, Z.-Q., Bao, Q., et al. (2017). Wafer-scale two-dimensional semiconductors from printed oxide skin of liquid metals. Nat. Commun. *8*, 14482.

Chiechi, R.C., Weiss, E.A., Dickey, M.D., and Whitesides, G.M. (2008). Eutectic gallium-indium (EGaIn): a moldable liquid metal for electrical characterization of self-assembled monolayers. Angew. Chem. Int. Ed. *47*, 142–144.

Clark, A.E., Wun-Fogle, M., and Restorff, J.B. (2000). Magnetostrictive properties of body-centered cubic Fe-Ga and Fe-Ga-Al alloy. IEEE Trans. Magn. *37*, 3238–3240.

Clark, A.E., and Belson, H. (1972). Giant room-temperature magnetostrictions in $TbFe_2$ and $DyFe_2$. Phys. Rev. *5*, 3642–3644.

Chechetka, S.A., Yu, Y., Zhen, X., Pramanik, M., Pu, K., and Miyako, E. (2017). Light-driven liquid metal nanotransformers for biomedical theranostics. Nat. Commun. *8*, 15432.

Chen, R., Romero, G., Christiansen, M.G., Mohr, A., and Anikeeva, P. (2015). Wireless magnetothermal deep brain stimulation. Science *347*, 1477–1480.

Chen, Y., Liu, Z., Zhu, D., Handschuh-Wang, S., Liang, S., Yang, J., Kong, T., Zhou, X., Liu, Y., and Zhou, X. (2017). Liquid metal droplets with high elasticity, mobility and mechanical robustness. Mater. Horiz. *4*, 591–597.

Chen, Y.Z., Zhou, T.J., Li, Y.Y., Zhu, L.F., Handschuh-Wang, S., Zhu, D.Y., Zhou, X.H., Liu, Z., Gan, T.S., and Zhou, X.C. (2018). Robust fabrication of nonstick, noncorrosive, conductive graphene-coated liquid metal droplets for droplet-based, floating electrodes. Adv. Funct. Mater. *28*, 1706277.

Chin, S.Y., Poh, Y.C., Kohler, A.-C., Compton, J.T., Hsu, L.L., Lau, K.M., Kim, S., BLee, B.W., Lee, F.Y., and Sia, S.K. (2017). Additive manufacturing of hydrogel-based materials for next-generation implantable medical devices. Sci. Robot. *2*, eaah6451.

Curley, S.A. (2003). Radiofrequency ablation of malignant liver tumors. Ann. Surg. Oncol. *10*, 338–347.

Dickey, M.D. (2014). Emerging applications of liquid metals featuring surface oxides. ACS Appl. Mater. Interfaces *6*, 18369–18379.

Diederich, C.J., and Hynynen, K. (1999). Ultrasound technology for hyperthermia. Ultrasound Med. Biol. *25*, 871–887.

Dunne, S.M., and Abraham, R. (2000). Dental post-operative sensitivity associated with a gallium-based restorative material. Br. Dent. J. *189*, 310–313.

Eaker, C.B., and Dickey, M.D. (2016). Reconfigurable water-substrate based antennas with temperature control. Appl. Phys. Rev. *3*, 031103.

Guan, A., Hamilton, P., Wang, Y., Gorbet, M., Li, Z., and Phillips, K.S. (2017). Medical devices on chips. Nat. Biomed. Eng. *1*, 0045.

Gough, R.C., Dang, J.H., Moorefield, M.R., Zhang, G.B., Hihara, L.H., Shiroma, W.A., and Ohta, A.T. (2016). Self-actuation of liquid metal via redox reaction. ACS Appl. Mater. Interfaces *8*, 6–10.

Haimbaugh, R.E. (2015). Practical Induction Heat Treating, Second Edition (ASM International).

Hergt, R., and Dutz, S. (2007). Magnetic particle hyperthermia—biophysical limitations of a visionary tumour therapy. J. Magn. Magn. Mater. *311*, 187–192.

Hussain, S.M., Hess, K.L., Gearhart, J.M., Geiss, K.T., and Schlager, J.J. (2005). *In vitro* toxicity of nanoparticles in BRL 3A rat liver cells. Toxicol. In Vitro *19*, 975–983.

Kaga, M., Nakajima, H., Sakai, T., and Oguchi, H. (1996). Gallium alloy restorations in primary teeth: a 12-month study. J. Am. Dent. Assoc. *127*, 1195–1200.

Karcher, C., Kocourek, V., and Schulze, D.. (2003). Experimental investigations of electromagnetic instabilities of free surfaces in a liquid metal drop. Presented at International Scientific Colloquium Modelling for Electromagnetic Processing, Hannover, March 24–26.

Khan, M.R., Trlica, C., So, J.H., Valeri, M., and Dickey, M.D. (2014). Influence of water on the interfacial behavior of gallium liquid metal alloys. ACS Appl. Mater. Interfaces *6*, 22467–22473.

Kim, D., and Lee, J.-B. (2015). Magnetic-field-induced liquid metal droplet manipulation. J. Korean Phys. Soc. *66*, 282–286.

Laurent, S., Bridot, J.L., Elst, L.V., and Muller, R.N. (2010). Magnetic iron oxide nanoparticles for biomedical applications. Future Med. Chem. *2*, 427–449.

Larsen, R.J., Dickey, M.D., Whitesides, G.M., and Weitz, D.A. (2009). Viscoelastic properties of oxide-coated liquid metals. J. Rheol. *53*, 1305–1326.

Liu, T.-Y., Chan, T.-Y., Wang, K.-S., and Tsou, H.-M. (2015). Influence of magnetic nanoparticle arrangement in ferrogels for tunable biomolecule diffusion. RSC Adv. *5*, 90098–90102.

Lu, Y., Hu, Q., Lin, Y., Pacardo, D.B., Wang, C., Sun, W., Ligler, F.S., Dickey, M.D., and Gu, Z. (2015). Transformable liquid-metal nanomedicine. Nat. Commun. *6*, 10066.

Matsuki, H., and Yanada, T. (1994). Temperature sensitive amorphous magnetic flakes for intratissue hyperthermia. Mater. Sci. Eng. A Struct. *181/A182*, 1366–1368.

O'Neal, D.P., Hirsch, L.R., Halas, N.J., Payne, J.D., and West, J.L. (2004). Photo-thermal tumor

ablation in mice using near infrared-absorbing nanoparticles. Cancer Lett. *209*, 171–176.

Pang, C.L.K. (2015). Hyperthermia in Oncology (CRC Press, Taylor & Francis).

Pankhurst, Q.A., Thanh, N.K.T., Jones, S.K., and Dobson, J. (2009). Progress in applications of magnetic nanoparticles in biomedicine. J. Phys. D Appl. Phys. *42*, 224001.

Sadghiani, N., Barbosa, L.S., Silva, L.P., Azevedo, R.B., Morais, P.C., and Lacava, Z.G.M. (2005). Genotoxicity and inflammatory investigation in mice treated with magnetite nanoparticles surface coated with polyaspartic acid. J. Magn. Magn. Mater. *289*, 466–468.

Salloum, M., Ma, R.H., Weeks, D., and Zhu, L. (2008). Controlling nanoparticle delivery in magnetic nanoparticle hyperthermia for cancer treatment: experimental study in agarose gel. Int. J. Hyperthermia *24*, 337–345.

Sheng, L., Zhang, J., and Liu, J. (2014). Diverse transformations of liquid metals between different morphologies. Adv. Mater. *26*, 6036–6042.

Shubitidze, F., Kekalo, K., Stigliano, R., and Baker, I. (2015). Magnetic nanoparticles with high specific absorption rate of electromagnetic energy at low field strength for hyperthermia therapy. J. Appl. Phys. *117*, 094302.

Singh, N., Jenkins, G.J.S., Asadi, R., and Doak, S.H. (2010). Potential toxicity of superparamagnetic iron oxide nanoparticles (SPION). Nano Rev. *1*, 5358.

Stafford, R.J., Shetty, A., Elliott, A.M., Schwartz, J.A., Goodrich, G.P., and Hazle, J.D. (2011). MR temperature imaging of nanoshell mediated laser ablation. Int. J. Hyperthermia *27*, 782–790.

Swallow, J.G., Kim, J.J., Maloney, J.M., Chen, D., Smith, J.F., Bishop, S.R., Tuller, H.L., and Vliet, K.J.V. (2017). Dynamic chemical expansion of thin-film non-stoichiometric oxides at extreme temperatures. Nat. Mater. *16*, 749–754.

Tang, S.-Y., Sivan, V., Khoshmanesh, K., O'Mullane, A.P., Tang, X., Gol, B., Eshtiaghi, N., Lieder, F., Petersen, P., Mitchell, A., and Kalantar-zadeh, K. (2013a). Electrochemically induced actuation of liquid metal marbles. Nanoscale *5*, 5949–5957.

Tang, X., Tang, S.-Y., Sivan, V., Zhang, W., Mitchell, A., Kalantar-zadeh, K., and Khoshmanesh, K. (2013b). Photochemically induced motion of liquid metal marbles. Appl. Phys. Lett. *103*, 174104.

Tang, S.-Y., Khoshmanesh, K., Sivana, V., Petersenb, P., O'Mullane, A.P., Abbott, D., Mitchell, A., and Kalantar-zadeh, K. (2014). Liquid metal enabled pump. Proc. Natl. Acad. Sci. USA *111*, 3304–3309.

Tayari, N., Heerschap, A., Scheenen, T.W.J., and Kobus, T. (2017). *In vivo* MR spectroscopic imaging of the prostate, from application to interpretation. Anal. Biochem. *529*, 158–170.

Thess, A., Votyakov, E.V., and Kolesnikov, Y. (2006). Lorentz force velocimetry. Phys. Rev. Lett. *96*, 164501.

Timko, B.P., Arruebo, M., Shankarappa, S.A., McAlvin, J.B., Okonkwo, O.S., Mizrahi, B., Stefanescu, C.F., Gomez, L., Zhu, J., Zhu, A., et al. (2014). Near-infrared–actuated devices for remotely controlled drug delivery. Proc. Natl. Acad. Sci. USA *111*, 1349–1354.

Tsai, J.T.H., Ho, C.-M., Wang, F.-C., and Liang, C.-T. (2009). Ultrahigh contrast light valve driven by electrocapillarity of liquid gallium. Appl. Phys. Lett. *95*, 251110.

Tufail, Y., Matyushov, A., Baldwin, N., Tauchmann, M.L., Georges, J., Yoshihiro, A., Tillery, S.I., and Tyler, W.J. (2010). Transcranial pulsed ultrasound stimulates intact brain circuits. Neuron *66*, 681–694.

Vogl, T.J., Nour-Eldin, N.A., Albrecht, M.H., Kaltenbach, B., Hohenforst-Schmidt, W., Lin, H., Panahi, B., Eichler, K., Gruber-Rouh, T., and Roman, A. (2017). Thermal ablation of lung tumors: focus on microwave ablation. Rofo *189*, 828–843.

Wang, Q., Yu, Y., Pan, K., and Liu, J. (2014). Liquid metal angiography for mega contrast X-ray visualization of vascular network in reconstructing *in-vitro* organ anatomy. IEEE Trans. Biomed. Eng. *61*, 2161–2166.

Wykes, R.C., Heeroma, J.H., Mantoan, L., Zheng, K., MacDonald, D.C., Deisseroth, K., Hashemi, K.S., Walker, M.C., Schorge, S., and Kullmann, D.M. (2012). Optogenetic and potassium channel gene therapy in a rodent model of focal neocortical epilepsy. Sci. Transl Med. *21*, 161ra152.

Yamaguchi, A., Mashima, Y., and Iyoda, T. (2015). Reversible size control of liquid-metal nanoparticles under ultrasonication. Angew. Chem. Int. Ed. *54*, 12809–12813.

Yoo, J.-W., Irvine, D.J., Discher, D.E., and Mitragotri, S. (2011). Bio-inspired, bioengineered and biomimetic drug delivery carriers. Nat. Rev. Drug Discov. *10*, 521–535.

Young, J.H., Wang, M.T., and Brezovich, I.A. (1980). Frequency/depth-penetration considerations in hyperthermia by magnetically induced currents. Electron. Lett. *16*, 358–359.

Yu, Y., and Miyako, E. (2017). Manipulation of biomolecules-modified liquid metal blobs. Angew. Chem. Int. Ed. *56*, 13606–13611.

Zavabeti, A., Daeneke, T., Chrimes, A.F., O'Mullane, A.P., Ou, J.Z., Mitchell, A., Khoshmanesh, K., and Kalantar-zadeh, K. (2016). Ionic imbalance induced self-propulsion of liquid metals. Nat. Commun. *7*, 12402.

Zhang, J., Yao, Y., Sheng, L., and Liu, J. (2015). Self-fueled biomimetic liquid metal mollusk. Adv. Mater. *27*, 2648–2655.

Zou, R., Zhang, Q., Zhao, Q., Peng, F., Wang, H., Yu, H., and Yang, J. (2010). Thermal stability of gold nanorods in an aqueous solution. Colloids Surf. A Physicochem. Eng. Asp. *372*, 177–181.

ISCI, Volume *3*

Supplemental Information

Alternating-Magnetic-Field-Mediated Wireless Manipulations of a Liquid Metal for Therapeutic Bioengineering

Yue Yu and Eijiro Miyako

Supplemental Figures

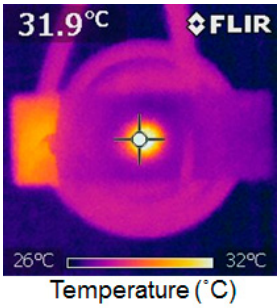

Fig. S1. Related to Fig. 1. Infrared image of LM (40 μL) heated by momentary ON–OFF switching of the AMF (250 A m^{-1}, 245 kHz).

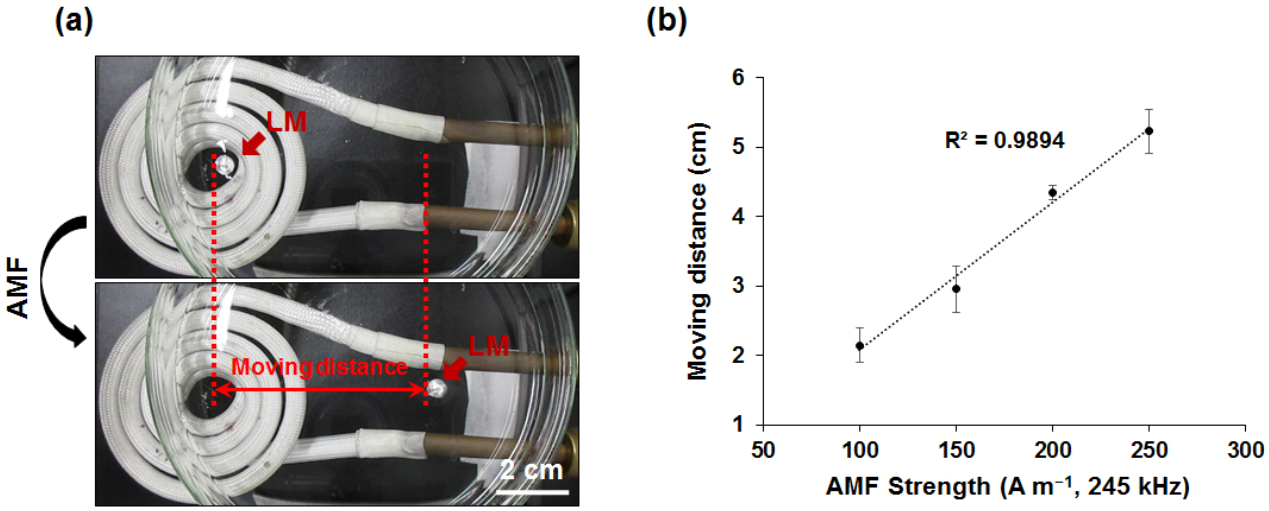

Fig. S2. Related to Fig. 2. Depiction (a) and statistics results (b) of LM moving distance by ON–OFF switching AMF. Data are represented as mean ± SEM.

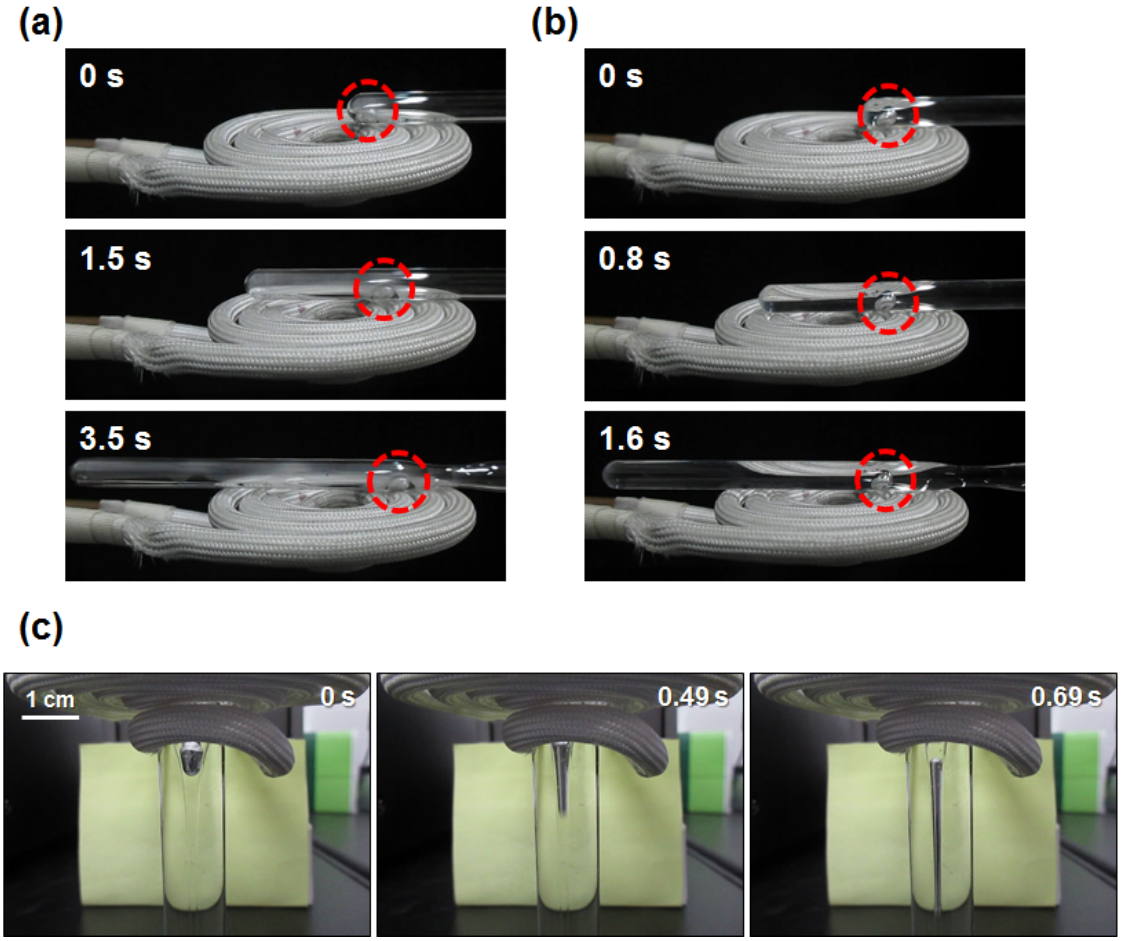

Fig. S3. Related to Fig. 2. Sequential snapshots of AMF-induced (100 A m^{-1}, 245 kHz) relative movement (to the glass tube) of LM blob (30 µL) (a) without or (b) with water. (c) Time-lapsed images revealing the flexible LM (30 µL) movement in a Pasteur pipette with water via AMF-induction (90 A m^{-1}, 245 kHz).

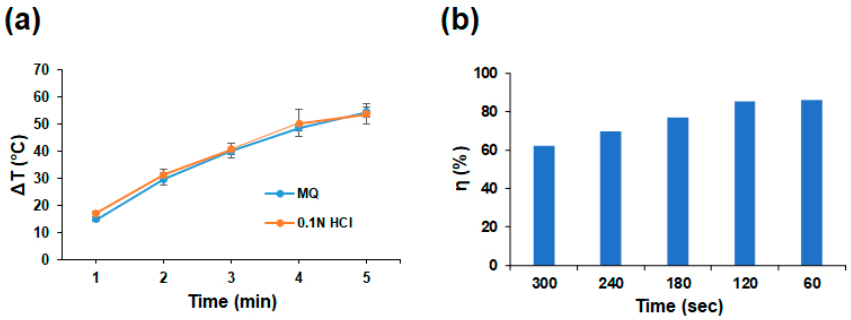

Fig. S4. Related to Fig. 3 and Experimental Procedures. (a) Temperature increasing curves of LM (30 µL) with or without oxidized layer in 5 mL media under AMF application (200 A m^{-1}, 245 kHz). Data are represented as mean ± SEM. (b) AMF−thermal conversion efficiency (η) of LM (30 µL) in MQ water (5 mL) after AMF application (200 A m^{-1}, 245 kHz) over a period of time (60, 120,180, 240 and 300 sec, respectivery).

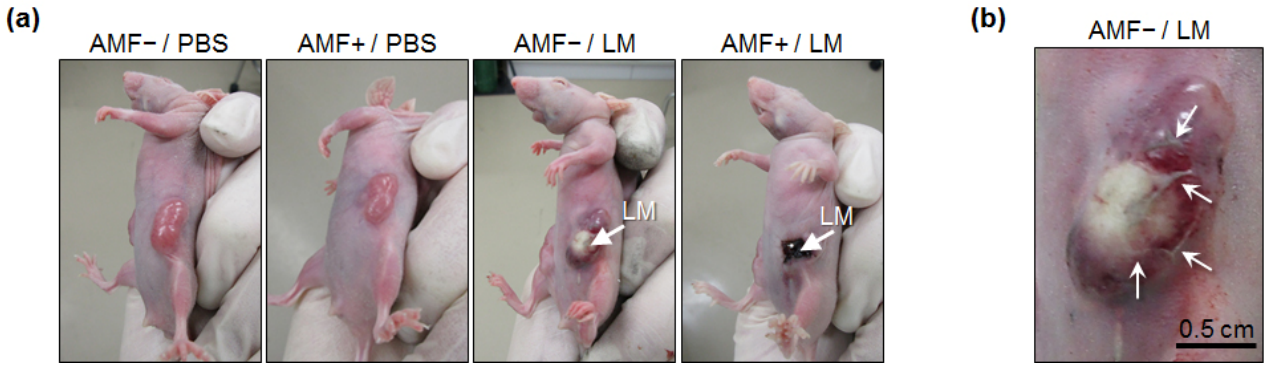

Fig. S5. Related to Fig. 5. (a) Representative images of a tumor injected with 30 μL of LM or PBS at 24 h post AMF treatment (150 A m^{-1}, 245 kHz). White arrows indicate the LM injection sites. (b) Representative image of tumor blood capillaries obstructed by the LM (white arrows).

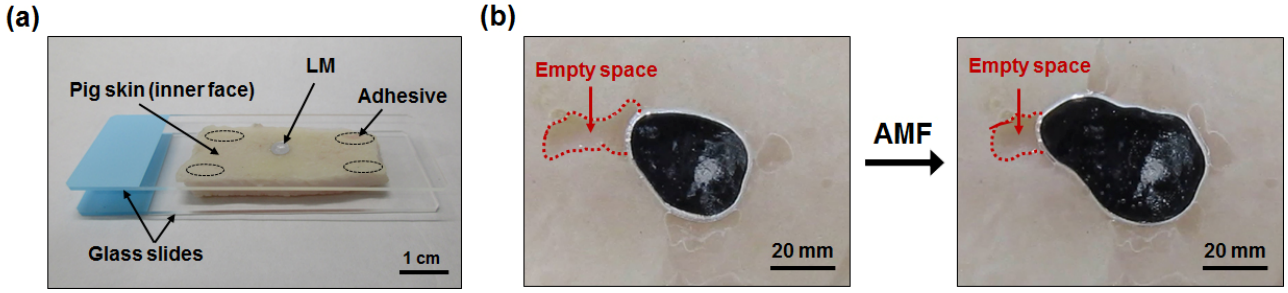

Fig. S6. Related to Figs. 4 and 5. AMF-induced LM transformation in *ex vivo* model. (a) Depiction of sandwich fabrication for simulation of AMF-induced LM subcutaneously transformation. (b) Transformation behavior of LM (30 μL) deposited between a glass slide and a piece of pig skin under AMF application (100 A m^{-1}, 245 kHz).

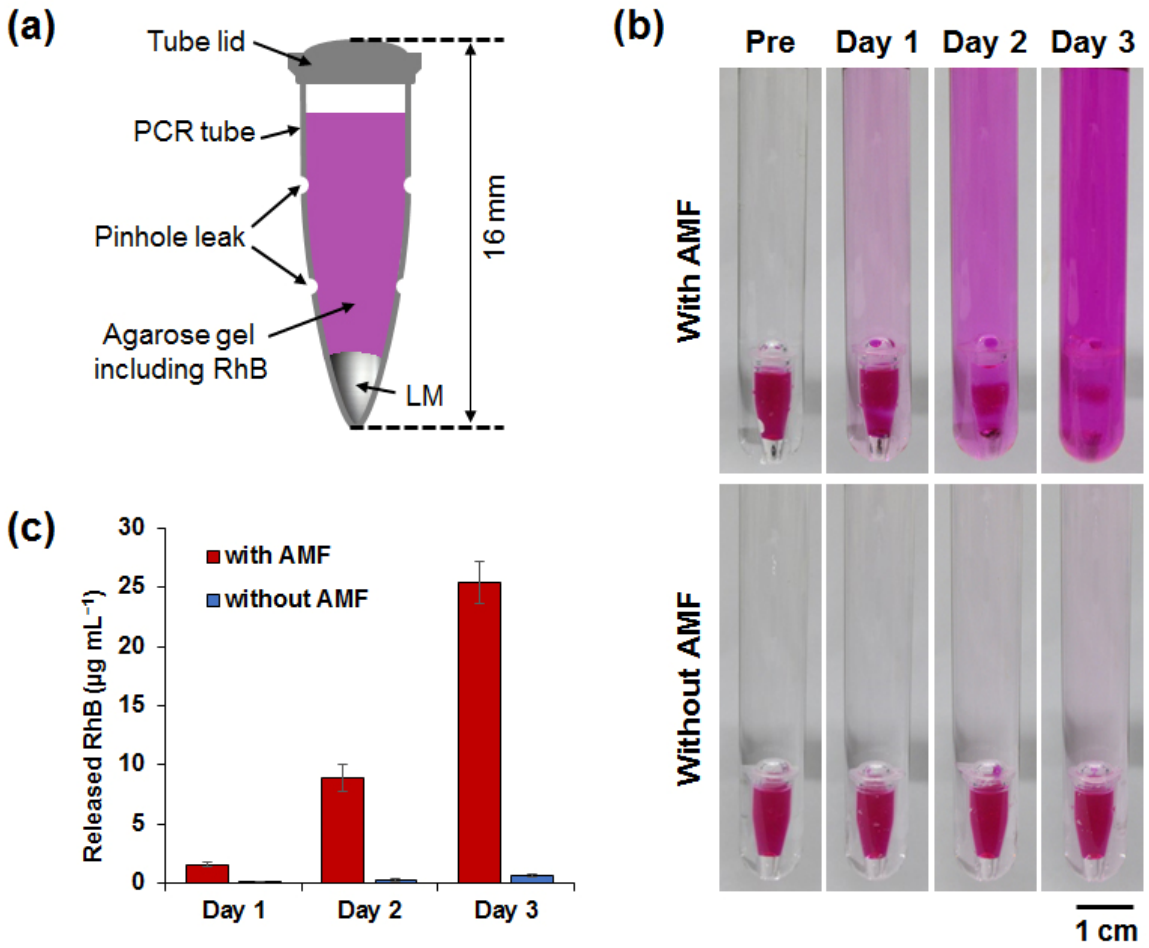

Fig. S7. Related to Fig. 6. (a) Depiction of LM/RhB-Gel capsule designed for long-termed drug (RhB) release. The capsule is composed of LM (30 μL), agarose (2%, w/w, 300 μL), RhB (1 mg mL^{-1}) and a PCR tube with four pinholes (diameter: 500 μm) on the wall. (b) Photographs and (c) quantitation of RhB release behavior from the capsule by AMF induction over 3 days. AMF (200 A m^{-1}, 245 kHz) was applied for 1 min once per day. Data are represented as mean ± SEM. The released RhB amount in water was determined by UV-vis absorption immediately after AMF induction. The system was kept at 37°C except when AMF was applied.

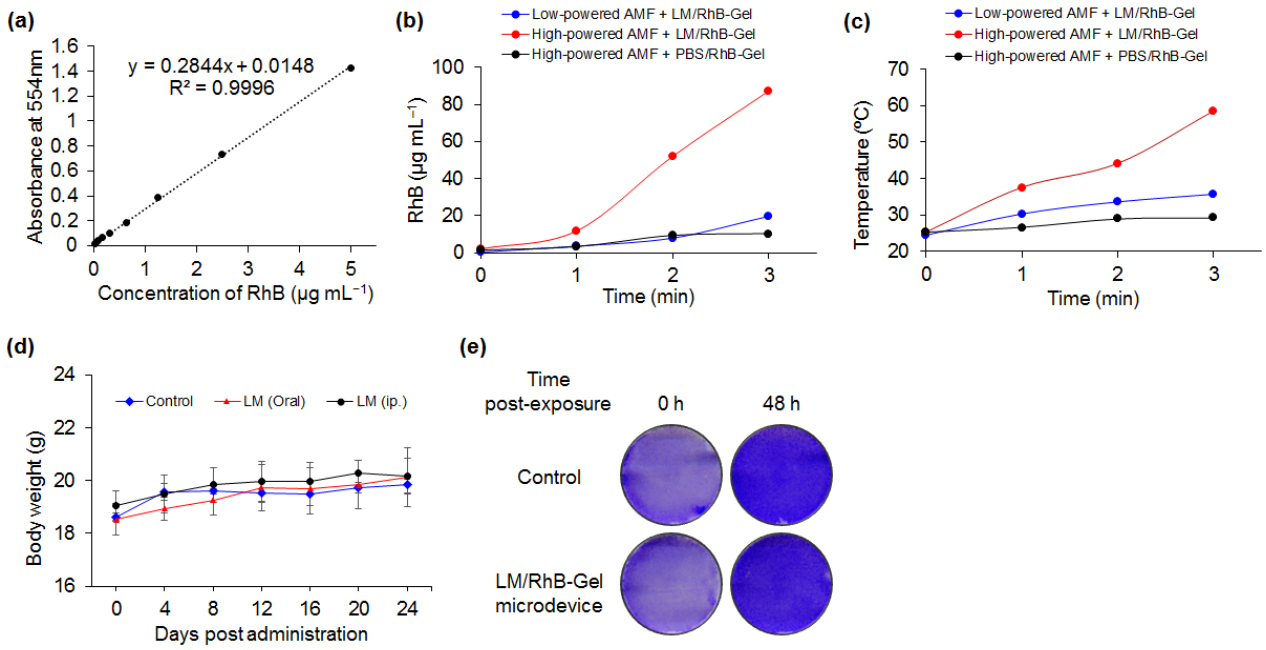

Fig. S8. Related to Fig. 6. (a) UV–vis calibration of RhB in water. (b) Release profile of RhB into 5 mL of water from the LM/RhB-Gel microdevice (LM 20 μL; 2% w w^{-1} agarose 200 μL; RhB, 0.5 mg mL^{-1}) under exposure to a low- (100 A m^{-1}, 245 kHz) or high-powered (100 A m^{-1}, 245 kHz) AMF over a period of time. The PBS/RhB-Gel microdevice in which the LM was replaced with the same amount of PBS served as the control. (c) Temperature increase of the LM/RhB-Gel microdevice immersed in 5 mL of water over period of time under exposure to a low- (100 A m^{-1}, 245 kHz) or high-powered (100 A m^{-1}, 245 kHz) AMF. The PBS/RhB-Gel microdevice with the LM replaced with the same amount of PBS served as the control. (d) Body weight of mice with different administrations of LM. Data are represented as mean ± SEM. (e) Crystal violet staining of TIG-3 with or without the LM/RhB-Gel microdevice under low-powered AMF exposure. Microdevices were incubated with cells in 3 mL of culture medium and were heated by an AMF (100 A m^{-1}, 245 kHz) for 2 min. Staining was performed immediately after treatment and 48 h later.

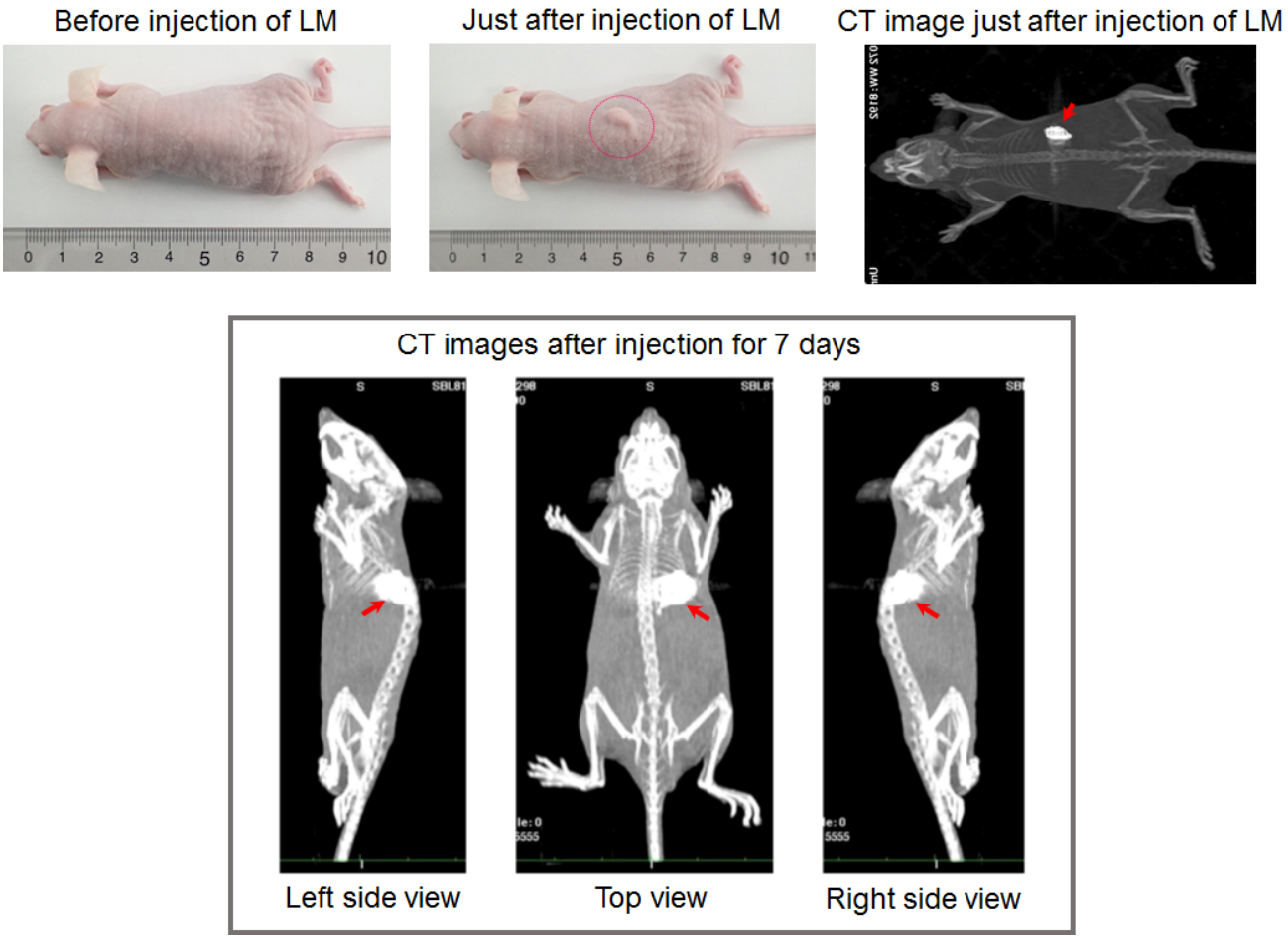

Fig. S9. Related to Fig. 6. Three-dimensional-X-ray images of LM (30 μL)-injected living mice (n = 4) immediately after subcutaneous administration and after injection for 7 days. Red circles indicate LM-injected site. Red arrows display the LM.

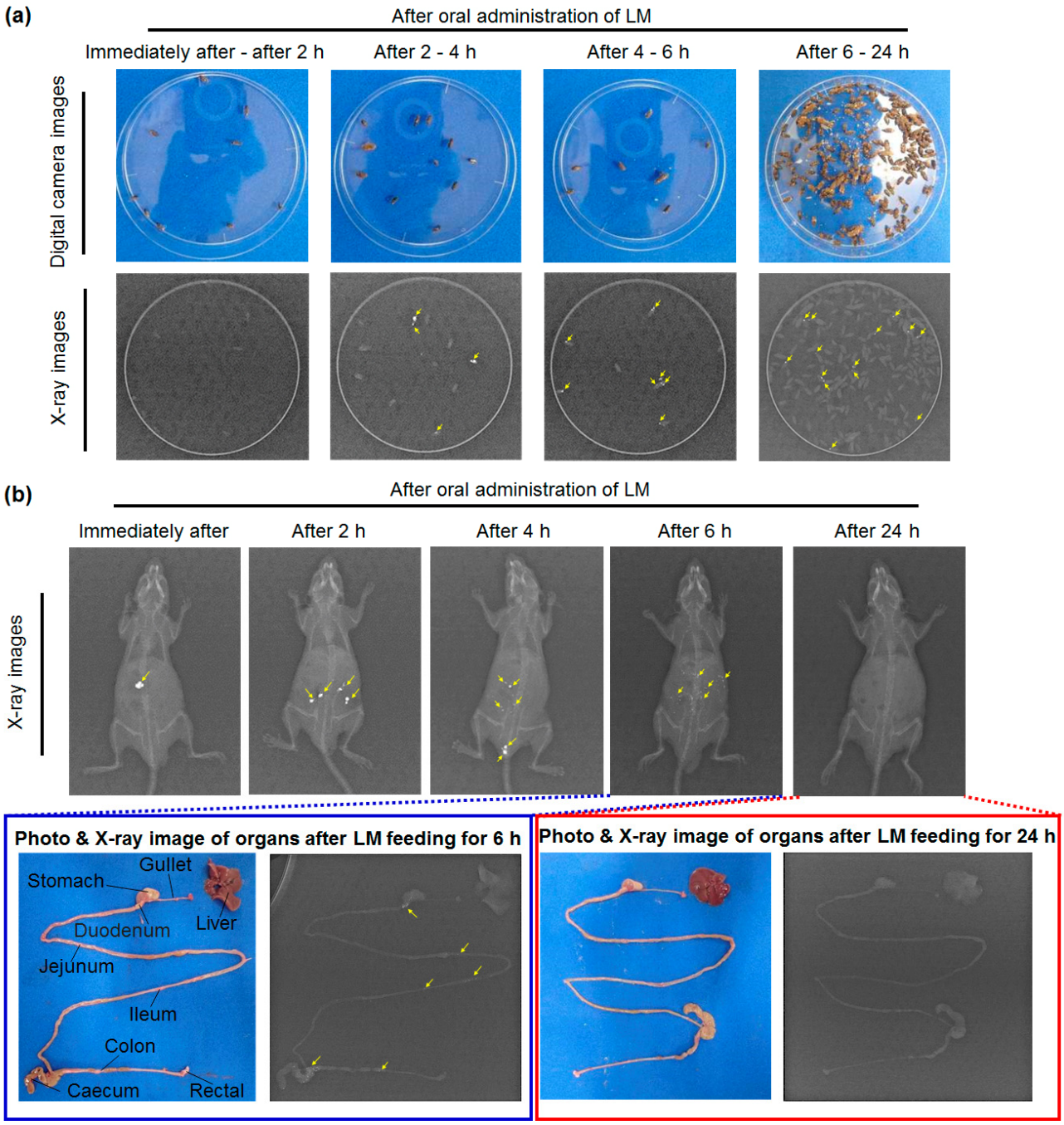

Fig. S10. Related to Fig. 6. X-ray images of LM (5 μL)-fed living mice (n = 3) after oral administration. (a) Photos and X-ray images of feces after oral feeding of LM for 24 h. (b) Photos and X-ray images of mice and organs after oral feeding of LM for 24 h.

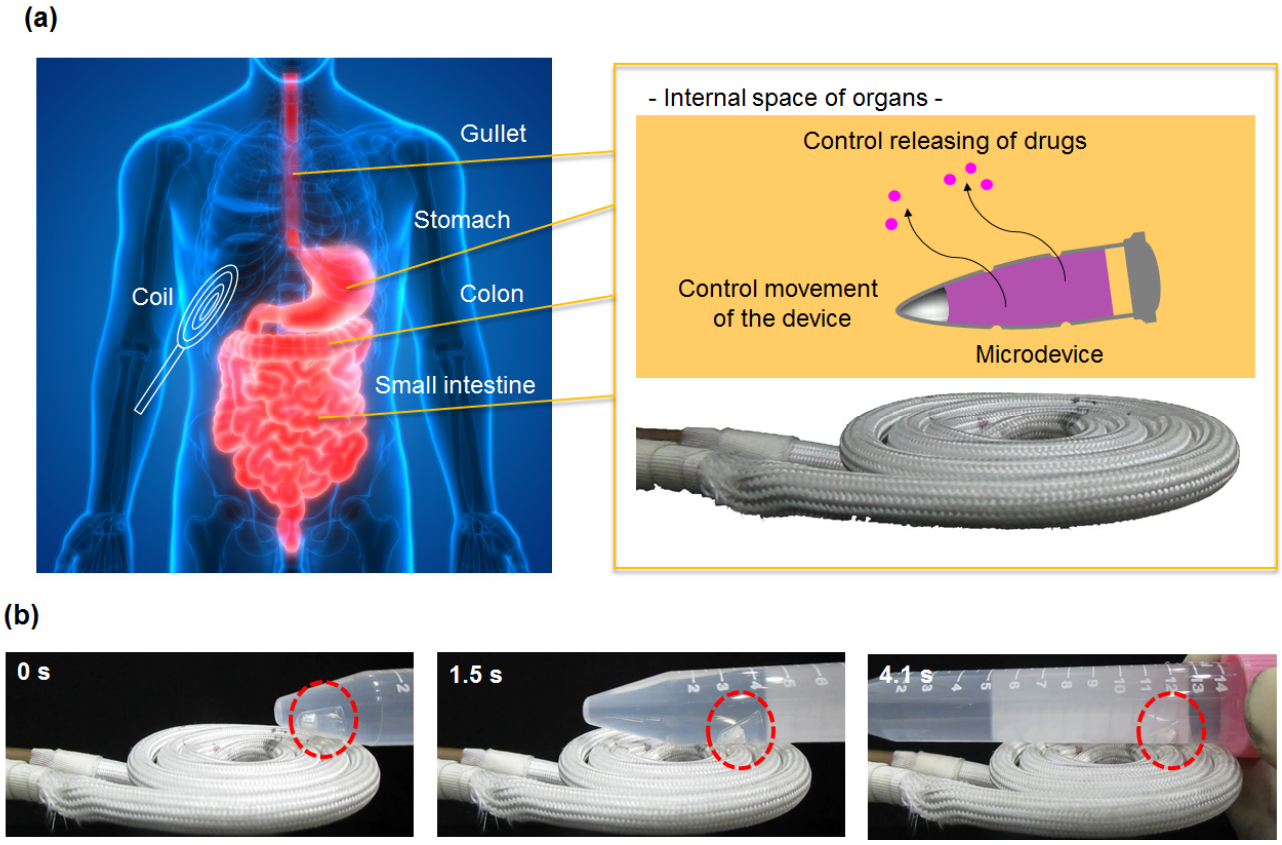

Fig. S11. Related to Fig. 6. (a) Schematic illustrations of utilities of LM/Gel microdevice in digestive organs for advanced drug delivery system, respectively. (b) Sequential snapshots of AMF-induced (100 A m^{-1}, 245 kHz) relative movement (to the falcon tube) of LM/Gel microdevice (LM 30 μL; 2% w/w agarose 200 μL) in PBS.

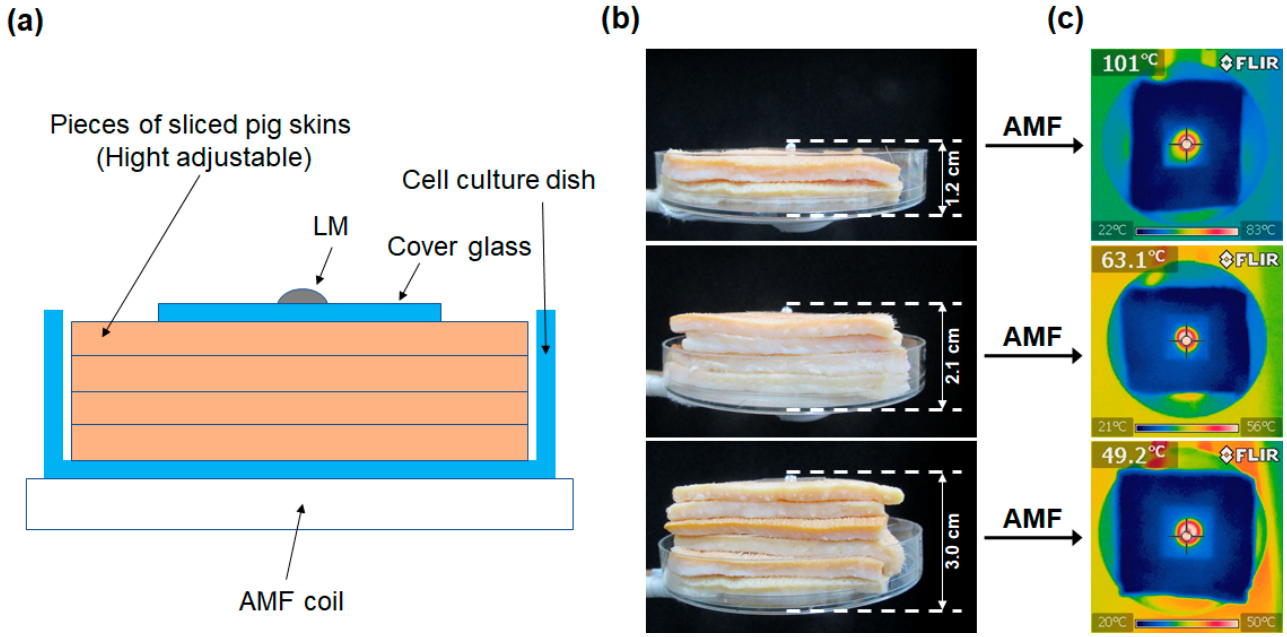

Fig. S12. Related to Fig. 6. Effect of AMF on depth penetration through biological tissues for LM heating. (a) Schematic illustration of the experimental set up. (b) LM (30 μL) was deposited on pig skins with different heights to AMF coil. (c) The thermal images of LM after AMF application (270 A m^{-1}, 245 kHz) for 10 seconds.

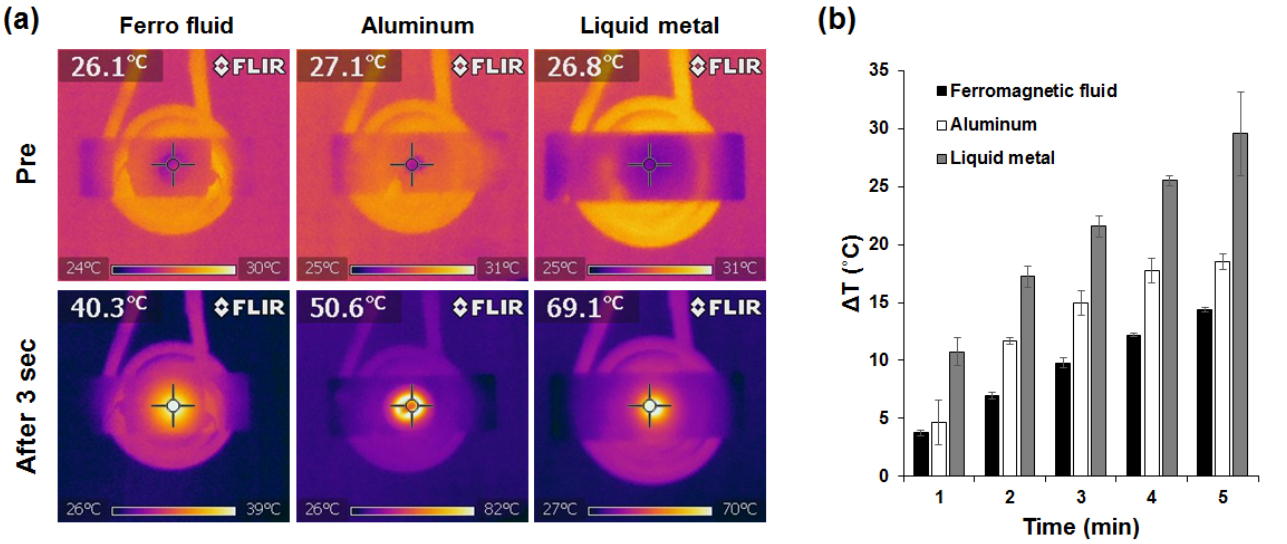

Fig. S13. Related to Figs. 3 and 6. (a) Thermal images of 100 mg of ferromagnetic fluid, aluminum and LM in air before and after AMF application (150 A m^{-1}, 245 kHz) for 3 sec. (b) Heating behavior comparison of various materials (100 mg) immersed in water (10 mL) over period of time under AMF exposure (200 A m^{-1}, 245 kHz). Data are represented as mean ± SEM.

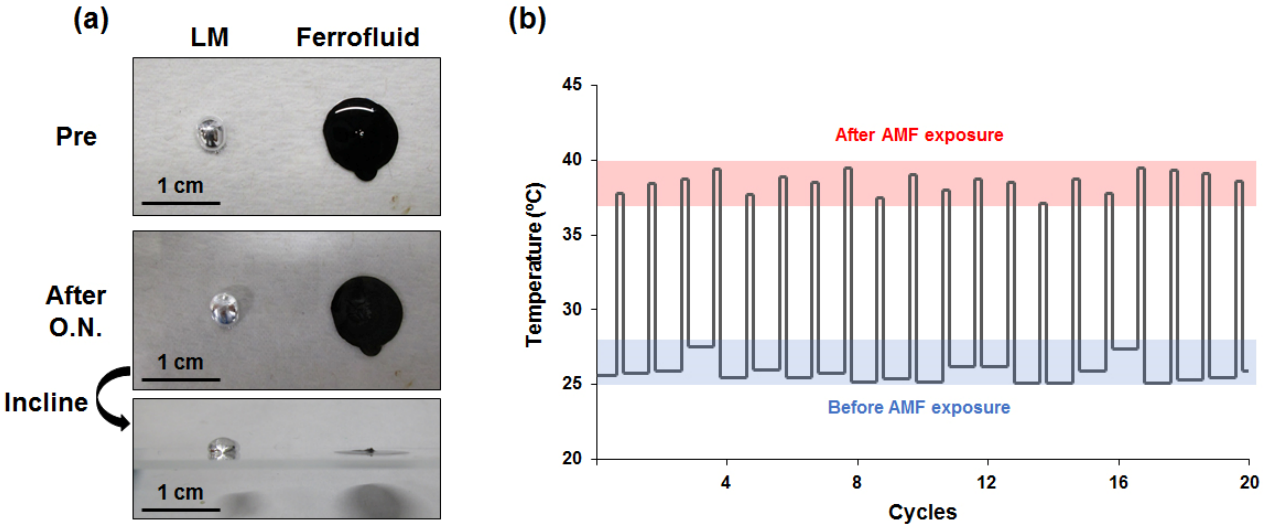

Fig. S14. Related to Figs.3 and 6. (a) Air-stable performance of LM and ferromagnetic fluid. Photographs showing 30 μL of LM and ferromagnetic fluid before and after being exposed to ambient air at room temperature for overnight. (b) LM thermal stability over 20 heating/cooling cycles. LM (50 μL) was immersed in PBS (10 mL) and exposed to AMF (200 A m^{-1}, 245 kHz) for 1 min. Temperatures before and after AMF exposure were recorded as one cycle.

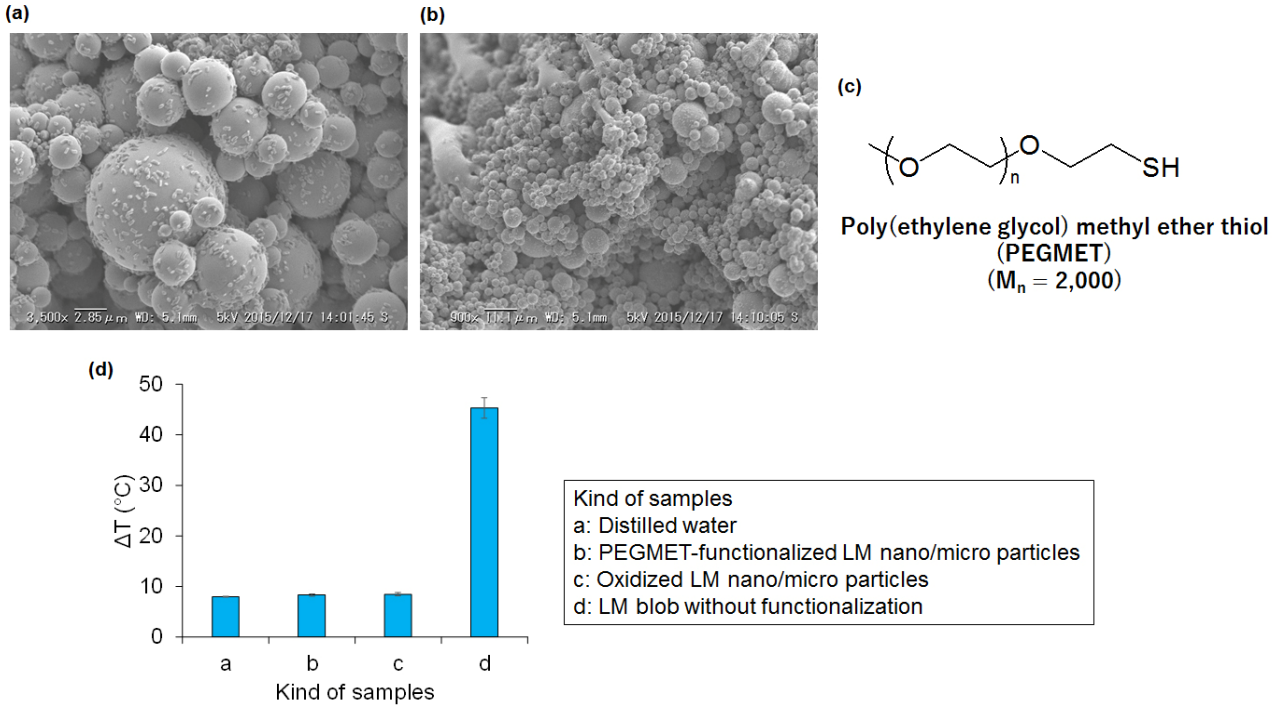

Fig. S15. Related to Figs. 3 and 6. SEM images of (a) oxidized LM nano/micro particles and (b) PEGMET-functionalized LM nano/microparticles. (c) Chemical structure of PEGMET. (d) AMF (270 A m^{-1}, 245 kHz)-induced temperature increasing behabiours of variusou LM samples in distilled water (5mL). LM concetration: 100 mg, AMF duration: 3 min. Data are represented as mean ± SEM.

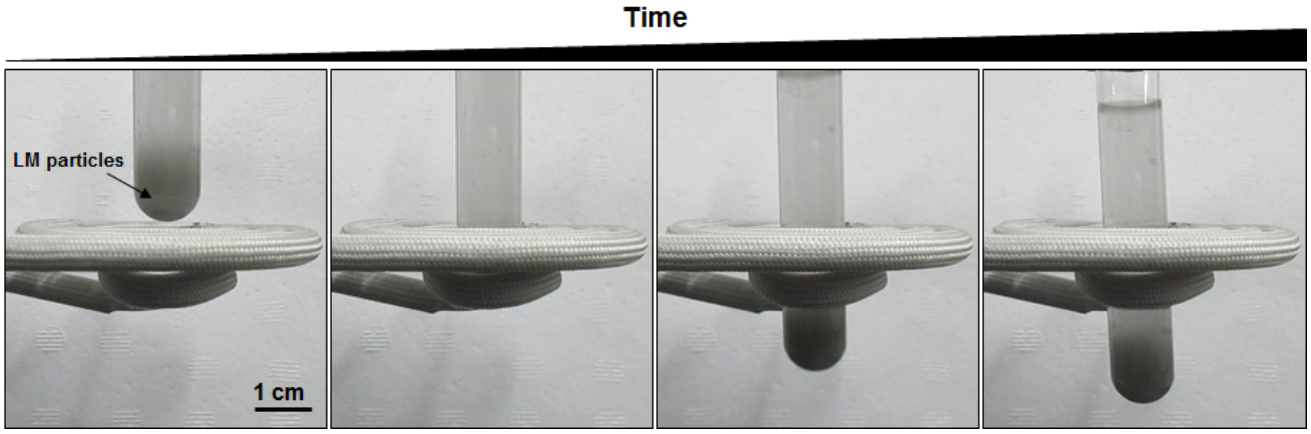

Fig. S16. Related to Figs. 1, 2 and 6. Sequeantial snapshots of LM nano/micro particles under AMF. LM: 100 mg in 5mL water, AMF: 250 A m^{-1}, 245 kHz.

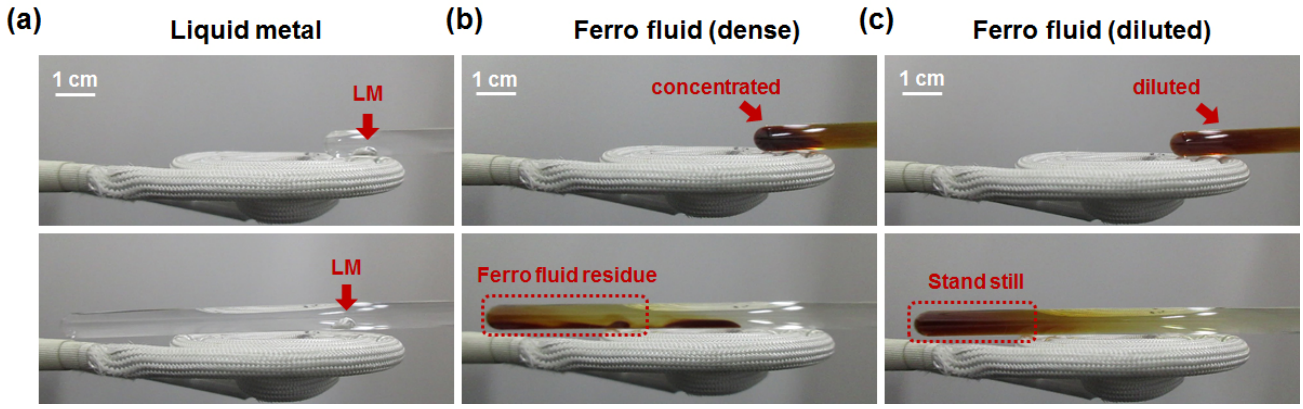

Fig. S17. Related to Figs. 1, 2 and 6. Sequential snapshots of AMF-induced (150 A m^{-1}, 245 kHz) relative movement (comparing to glass tube) of (a) LM blob, (b) dense and (c) diluted ferro fluids in the aqueous solution.

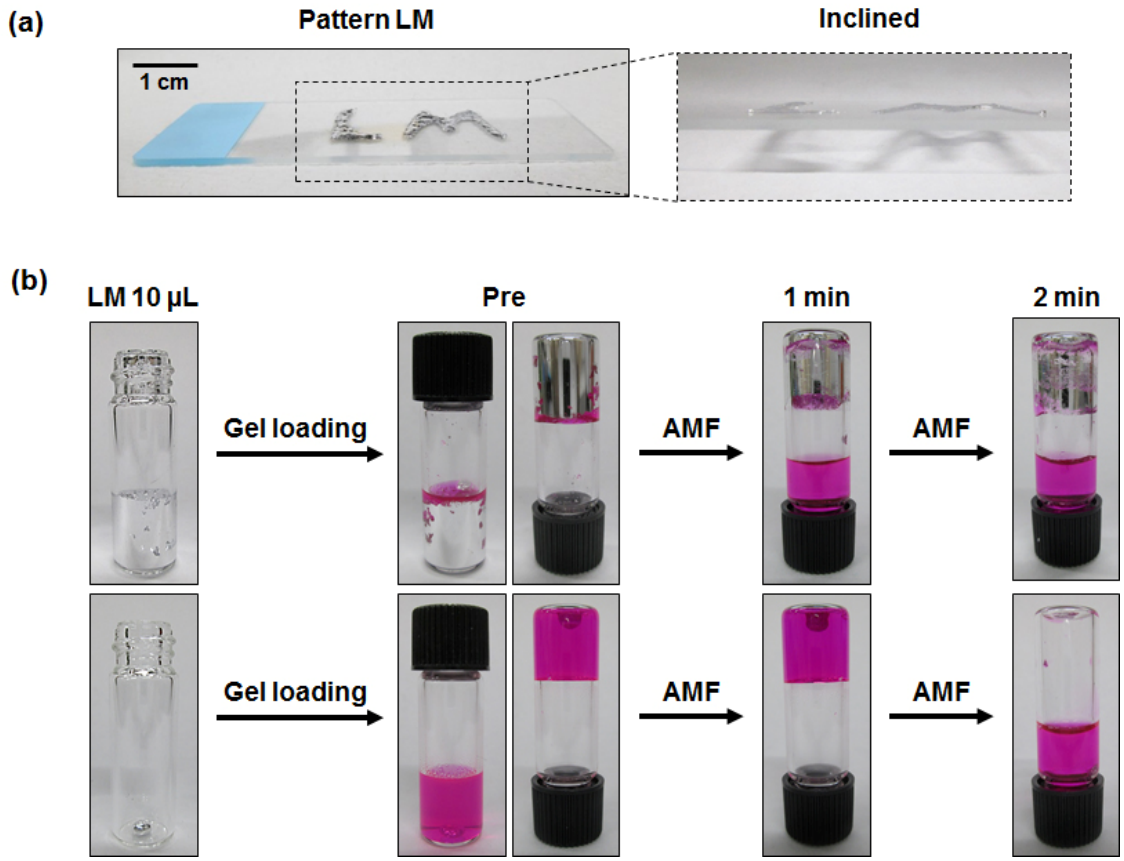

Fig. S18. Related to Fig. 6. (a) Patterning LM layer (50 μL totally) on a glass slide. (b) Drug releasing behabiours in comparison with LM in different forms (spherical droplet and spreading layer) under AMF. LM: 10 μL, hydrogel matrix: 500 μL (agarose: 2% w w^{-1}; RhB, 0.1 mg mL^{-1}), AMF: 150 A m^{-1}, 245 kHz.

Table S1 Related to Fig. 6. Complete blood cell count (CBC) and biochemical examination after 28 days*.

Methods	Entry**	Unit	Subcutaneous injection (n = 5)		
			LM	PBS	p value
CBC	WBC	$\times 10^2\ \mu L^{-1}$	71.8 ± 5.3	75.4 ± 15.4	> 0.05
	RBC	$\times 10^4\ \mu L^{-1}$	901.4 ± 37.6	894.2 ± 13.3	> 0.05
	HGB	$g\ dL^{-1}$	14.1 ± 0.6	14.2 ± 0.3	> 0.05
	HCT	%	41.5 ± 1.9	41.3 ± 0.5	> 0.05
	MCV	fL	46.0 ± 0.4	46.2 ± 0.3	> 0.05
	MCH	pg	15.7 ± 0.1	15.8 ± 0.3	> 0.05
	MCHC	$g\ dL^{-1}$	34.0 ± 0.4	34.3 ± 0.4	> 0.05
	PLT	$\times 10^4\ \mu L^{-1}$	70.4 ± 4.2	70.8 ± 5.9	> 0.05
Biochemical exam	CRP	$\mu g\ mL^{-1}$	1.3 ± 0.1	1.6 ± 0.5	> 0.05
	AST	$IU\ L^{-1}$	59.8 ± 10.7	77.8± 31.9	> 0.05
	ALT	$IU\ L^{-1}$	33.0 ± 5.2	36.2 ± 14.2	> 0.05
	LDH	$IU\ L^{-1}$	246.0 ± 77.3	325.8 ± 138.3	> 0.05
	AMY	$IU\ L^{-1}$	1723.4 ± 156.0	1654.0 ± 179.1	> 0.05
	CK	$IU\ L^{-1}$	164.0 ± 54.4	231.0 ± 179.0	> 0.05
	TP	$g\ dL^{-1}$	4.1 ± 0.1	4.0 ± 0.1	> 0.05
	ALB	$g\ dL^{-1}$	2.8 ± 0.1	2.7 ± 0.2	> 0.05
	CRE	$mg\ dL^{-1}$	0.1 ± 0.01	0.1 ± 0.02	> 0.05

*The date shows average values from five experiments. Values in brackets indicate standard deviation.

**Abbreviations: WBC (white blood cell), RBC (red blood cell), HGB (hemoglobin), HCT (hematocrit), MCV (mean corpuscular volume), MCH (mean corpuscular hemoglobin), MCHC (mean corpuscular hemoglobin concentration), PLT (platelet), CRP (C-reactive protein), AST (aspartate aminotransferase), ALT (alanine aminotransferase), LDH (lactate dehydrogenase), AMY (amylase), CK (creatine kinase), TP (total protein), ALB (albumin), CRE (creatinine). Results were presented in the form of mean ± standard deviation, with “n” indicating the number of samples per group. Statistical analyses were performed using Student’s t-tes

Transparent Methods

AMF-induced temperature increase

All heat-dissipation experiments were performed using an EasyHeat device (Ambrell, NY, USA) consisting of a transistor inverter and a sample coil enclosure powered by an AC power supply. AMF-induced temperature increases were investigated as follows. A droplet of LM (Ga:In = 75.5:24.5 wt%; Alfa Aesar, Ward Hill, MA, USA) (25 μL, ~100 mg) was immersed into distilled water (5 mL) followed by AMF exposure under various conditions as indicated. The temperature of the solutions was measured in real time using a temperature sensor (AD-5601A; A&D, Tokyo, Japan). The LM droplet surface temperature after AMF heating was monitored by infrared (IR) thermography (i7; FLIR, Nashua, NH, USA).

For the heating stability and comparison experiments, the same methods mentioned above was performed with ferrofluid [sodium tetradecene sulfonate-functionalized magnetite (Fe_3O_4) nanoparticles, concentration of Fe_3O_4 is 35 wt%, diameter of nanoparticles is about 10 nm, and solvent is distilled water] (M-300, Sigma Hi-Chemical, Kanagawa, Japan), Aluminum foil (0070, Toyo Aluminum Ekco Products, Osaka, Japan) and LM under the conditions as indicated.

LM micro/nano particles were prepared by the following way. Briefly, LM (25 μL, ~100 mg) was mixed in distilled water (10 mL) by pulse-type sonication (VCX-600; Sonics, Danbury, CT, USA) for 10 min in ice bath with and without poly(ethylene glycol) methyl ether thiol (PEGMET) [number-average molecular weight M_n = 2,000; Aldrich, MO, USA) (10 mg)]. The product (LM concentration: ~20 mg mL^{-1}) was then used for further structural and exothermic characterizations. The structure of LM micro/nano particles with and without poly(ethylene glycol) methyl ether thiol was observed by a scanning electron microscopy (SEM) (VE-9800; Keyence, Osaka, Japan).

AMF−thermal conversion efficiency of LMs was determined according to the previous methods (Yonetsu et al., 2014; Ikemoto et al., 1986). Detailed calculation was given as following:

$$\eta = CVD(T2 - T1) / Pt \quad (1)$$

where η is the AMF−thermal conversion efficiency, C is the heat capacity of EGaIn (0.38 J g^{-1} °C^{-1}) (Majeski et al., 2010; Yu et al., 2014), V is the volume of EGaIn blob (3×10^{-8} m^3), D is the density of EGaIn (6.25×10^6 g m^{-3}) (Xu et al., 2012), and t is the heating time (60 sec). The attainment temperature (T2) of the distilled water of the LM blob after 60 sec was 35.1°C and initial temperature (T1) was 20.0°C. Herein, the temperature change (T2 – T1) of the water of the LM blob was 15.1°C.

The value of the power for heating (P) is defined as equation (2).

$$P \approx \frac{B^2 f^2}{R} \quad (2)$$

The magnetic flux density (B) can be calculated by equation (3). Meanwhile, f is the frequency of AMF (245×10^3 Hz). R is the electrical resistivity of water (18.3×10^4 Ω) (Kaye, G.W.C. et al., 1911).

$$B = \mu H \quad (3)$$

Where μ is the magnetic permeability of water (12.6×10^{-7} H m^{-1}) (Kaye, G.W.C. et al., 1911) and H is the magnetic field strength (200 A m^{-1}). The values of V, t, T_{atta}, T_{ini}, f, and H were obtained from Figure S4a.

Thus, substituting according values of each parameter to equation (1), AMF−thermal conversion efficiency (η) of the LM droplets can be calculated to be about 86.3%. The efficiencies at different times were also calculated by

the same way and summarized in Figure S4b.

Cell culture and viability assays

Human lung carcinoma (A549), colorectal adenocarcinoma (HT-29), bone osteosarcoma (U2OS), and normal diploid fibroblasts (TIG3) were obtained from JCRB Cell Bank or DS Pharma Biomedical (Tokyo, Japan) and cultured in Dulbecco's Modified Eagle's medium (DMEM) medium (Gibco BRL, Grand Island, NY, USA) with 10% fetal bovine serum, 2 mM L-glutamine, 1 mM sodium pyruvate, gentamycin, penicillin–streptomycin (100 IU mL^{-1}), and Hank's balanced salt solution (Life Technologies, MD, USA). Cells were maintained at 37°C in a humidified chamber at 5% CO_2.

Cell viability assays were conducted by crystal violet staining (Wako, Osaka, Japan) and using Cell Counting Kit-8 (CCK-8; Dojindo Laboratories, Kumamoto, Japan). For the crystal violet assays, cells were seeded in 6-well (2.5×10^5 cells $well^{-1}$) or 12-well (1.5×10^5 cells $well^{-1}$) plates the night before the treatment. After cell attachment, a LM droplet (25 µL) or the LM-Gel microdevice was added to the wells, followed by AMF exposure for the indicated period. The staining was carried out either immediately after the treatment or 24 h later. Prior to staining, the LM was removed and the cells were washed with cold PBS and fixed with a pre-chilled methanol/acetone (1:1) mixture for 10 min. The fixed cells were then incubated with 0.1% crystal violet solution overnight. For CCK-8 assays, cells were seeded in 24-well (5×10^4 cells $well^{-1}$) or 48-well (2×10^4 cells $well^{-1}$) plates. After 24 h, a 20-µL droplet of the LM was added for the as-indicated AMF treatment. After the LM was removed, the cells were washed with fresh medium and then incubated with CCK-8 solution according to the manufacturer's instructions. Absorbance at 450 nm was read on a microplate reader (Infinite M200 PRO, Tecan, Männedorf, Switzerland). All assays were performed independently at least three times.

***In vivo* magnetic hyperthermia therapy**

All animal experiments were performed strictly in accordance with protocols approved by the Institutional Animal Care and Use Committee of AIST. The HT-29 tumor-bearing C57BL/6NCrSlc mice (n = 5, female, 5 weeks old; Japan SLC, Shizuoka, Japan) were intratumorally injected with 30 µL of the LM when the tumor volumes reached approximately 250 mm^3. An equal volume of PBS buffer solution was applied as a control. Subsequently, the mice were exposed to an AMF (150 A m^{-1}, 245 kHz) for 5 min. During the AMF treatment, the temperature at the tumor site was measured by IR thermography. Tumor formation and mice health (body weight) was monitored every other day. The volume of the subcutaneous tumors was calculated as $V = L \times W^2/2$, where L and W are the length and width of the tumor, respectively.

***In vivo* viability evaluation**

Five-week-old female mice (n = 5; average weight = 18 g; C57BL/6NCrSlc) were provided by Japan SLC, Inc. (Shizuoka, Japan) and housed in a specific pathogen-free environment. Two hundred microliters of LM suspension (10 mg mL^{-1}, sonicated in PBS for 10 min) was administered to the mice by either oral feeding or intraperitoneal injection. The body weights of the mice were recorded every other day for 24 days.

Further LM biocompatibility tests were investigated as follows. LM or PBS was injected into the tail vein and

the back under the skin of a 10-week-old female mouse (n = 5; average weight = 21 g; BALB/cSlc; Japan SLC, Inc.). Volumes of injected LMs for subcutaneous administrations was 30 μL. Viability observations and weight determinations of injected mice were performed every twice a week for 60 days. Blood samples were collected from the inferior vena cava of the mouse after 28 days. CBC and biochemical examination were performed by Japan SLC, Inc. and Oriental Yeast Co., Ltd. (Tokyo, Japan).

The distribution behavior of injected LMs in living mice was analysed by Shin Nippon Biomedical Laboratories, Ltd. (Kagoshima, Japan) using the X-ray CT instrument (Asteion/S4; Toshiba Medical Systems, Tochigi, Japan). LM (30 μL) was subcutaneously injected into the back of 11-week-old male nude mice (n = 4; average weight = 21 g; BALB/cAJc-nu/nu, Japan SLC, Inc.). X-ray CT scanning was performed under anaesthesia of mice just after injection or after incubation for 7 days with injection. For biological distribution of LM via oral administration, five microliters of LM was administered to the 11-week-old male mice (n = 3; average weight = 22 g; BALB/cAJlc-nu/nu, Japan SLC, Inc.) by oral feeding. X-ray CT imaging of the mice, feces, and organs were performed for 24 h.

Simulation of AMF-induced subcutaneous LM transformation

A sandwich system consisted of glass slide – pig skin tissue – glass slide (from bottom to top) was assembled as shown in Figure S5. Briefly, 30 μL of LM was deposited on the inner face of pig skin (ca. 4 cm × 2.5 cm, Funakoshi, Tokyo, Japan) attaching on the bottom slide. The corners of the skin were subsequently coated with instant adhesive, so that the following top slide can be tightly covered on the skin. After 10 min for adhesive stabilization, the packed sandwich system was subjected to AMF exposure (100 A m^{-1}, 245 kHz) to observe the LM transformation.

Controlled release of RhB

The RhB (Wako)-loaded LM/hydrogel system was subjected to an aqueous environment to investigate AMF-induced RhB release. The aqueous solution volumes and AMF conditions were adjustable depending on the purposes of the experiment. In the case of RhB release in a glass vial, 2 mL of Milli-Q water was added to the LM/hydrogel depot (LM 20 μL; agarose 2% w w^{-1}; RhB 0.5 mg mL^{-1}) with a solidified volume of 1 mL; the vial was then placed on the coil for AMF exposure (200 A m^{-1}, 245 kHz). The AMF exposure time was set to 30 s for ON and 30 s for OFF, and the exposure was repeated for five cycles. At each interval, the temperature of the LM/hydrogel and the surrounding water was measured using a temperature sensor, whereas 10 μL of supernatant was collected for calculation of the release rate. The RhB release rate in the presence or absence of the AMF was measured on the basis of the concentration of released RhB calculated from the UV–Vis calibration curve in Figure S3a. The same RhB-loaded hydrogel depot without LM (replaced with PBS) was used as a negative control. For the long-termed RhB release experiment, the system was kept at 37°C for 3 days except when AMF was applied (1 min once per day).

Fabrication of the LM/hydrogel system

The volumes of agarose (Wako), LM, and RhB were adjusted depending on the type of container (glass vial or PCR tube). For instance, a LM/RhB-Gel microdevice was fabricated by dissolving 0.5 g of agarose in 25 mL of RhB aqueous solution (0.5 mg mL^{-1}) at 60°C, followed by vortex mixing. Then, 200 μL of molten agarose mixture was transferred into a PCR tube (ca. 2000 μm in length and 500 μm in width, Eppendorf, Hamburg, Germany) together

with 20 μL of the LM. The PCR tube was chilled at room temperature until the LM-loaded hydrogel depot solidified. The resultant fabricated drug delivery microdevice was enclosed with the PCR tube cap and stored at 4°C prior to further experiments.

References

Ikemoto, Y., Takahashi, A., and Hama, H. (1986). Temperature distribution of flying pan heated with a magnetic induction heating cooker and it thermal efficiency. Kaseigakuzashi *37*, 949–954.

Kaye, G.W.C., and Laby, T.H. (1911) Table of physical and chemical constants and some mathematical functions. National Physical Laboratory.

Majeski, R. (2010). Liquid metal walls, lithium, and low recycling boundary conditions in tokamaks. AIP Conf. Proc. *1237*, 122.

Yonetsu, D., and Yamamoto, Y. J. (2014). Caluculation of heating efficiency of induction heating cooker by using finite element analysis. IEIE Jpn. *34*, 339–345.

Yu, S., and Kaviany, M., (2014). Electrical, thermal, and species transport properties of liquid eutectic Ga-In and Ga-In-Sn from first principles. J. Chem. Phys. *140*, 064303.

Xu, Q., Oudalov, N., Guo, Q., Jaeger, H.M., and Brown, E. (2012). Effect of oxidation on the mechanical properties of liquid gallium and eutectic gallium-indium. Phys. Fluids *24*, 063101.